Earth, Moon, and Planets (2022) 126:2
https://doi.org/10.1007/s11038-021-09544-0

Photometric Correction of Images of Visible and Near-Infrared Bands from Chandrayaan-1 Hyper-Spectral Imager (HySI)

HySI Photometric Correction

Subhadyouti Bose[1] · **Mili Ghosh Nee Lala**[1] · **Akhouri Pramod Krishna**[1]

Received: 6 March 2021 / Accepted: 18 November 2021 / Published online: 6 December 2021

Abstract
Photometric correction is a necessary step in planetary image pre-processing since the images of planetary surfaces are acquired by orbiting spacecraft at various observational geometries. In this study, visible (748 nm) and near-infrared (948 nm) bands of Hyper Spectral Imager (HySI) onboard Chandrayaan-1 have been used to derive a preliminary photometric correction for lunar data. The purpose of the proposed photometric correction for HySI is to convert observations taken at solar incidence (i), sensor emission (e), and the solar phase angles (α) to a fixed geometry by applying $i = \alpha = 30°$ and $e = 0°$ to each image. The Lommel–Seeliger function was used to model the lunar limb darkening effect, while topography data from the merged Digital Elevation Model of Lunar Reconnaissance Orbiter—Lunar Orbiter Laser Altimeter (LRO-LOLA) and SELENE Terrain Camera (TC) was used to correct local topographic effects. Data from Moon Mineralogy Mapper (M^3), SELENE Multiband Imager (MI) and Clementine Ultraviolet and Visible Camera (UV/VIS) were also used to compare radiance, reflectance and phase functions derived from HySI. Our analysis reveals that HySI is darker than M^3 primarily due to low surface radiance conditions observed by HySI. The derived phase functions for the two HySI bands indicate a good correlation between the derived reflectance and phase angle as well as with the phase functions derived for the empirically corrected M^3 data. This approach led to the derivation of a photometric correction for maria regions. Finally, it is expected that the proposed correction would be applicable to all HySI images covering the lunar mare region.

Keywords Image processing · Moon · Moon surface · Photometry

1 Introduction

Chandrayaan-1 is India's first mission to the Moon and the vast amount of data obtained from its various instruments have been used to study the lunar surface morphology, (e.g., Arya et al. 2018; Cheek et al. 2011; Kaur et al. 2013; Kramer et al. 2011; Srivastava and

✉ Subhadyouti Bose
subha.bose.geoscience@gmail.com

[1] Department of Remote Sensing, Birla Institute of Technology, Mesra, Ranchi 835215, India

Varatharajan 2016), the diverse surface mineralogy, (e.g., Bhattacharya et al. 2011, 2015; Isaacson et al. 2011; Staid et al. 2011; Varatharajan et al. 2014; Zhang et al. 2016) and search for evidences of water on the surface (e.g., Bhattacharya et al. 2013; Li et al. 2018; Li and Milliken 2017; Milliken and Li, 2017; Pieters et al. 2009a, b; Sridharan et al. 2010). Among the various scientific instruments onboard Chandrayaan-1 were the high-resolution Terrain Mapping Camera (TMC) (Kiran Kumar et al. 2009a; Kiran Kumar and Chowdhury 2005a), Hyper Spectral Imager (HySI) (Kiran Kumar et al. 2009b; Kiran Kumar and Chowdhury 2005b) and Moon Mineralogy Mapper (M^3) (Pieters et al. 2009a), which were specifically designed to study the surface of the Moon in the visible to near-infrared range of the electromagnetic (EM) spectrum, at very high spatial and spectral resolutions.

Remote observations of the lunar surface involve the acquisition of images with different viewing geometries which can be expressed by three angles namely, incidence angle 'i', emission angle 'e' and, the solar phase angle 'α'. These angles are determined based on the positioning of the spacecraft above the lunar surface and the angle at which the solar radiation hits the lunar surface. Since images from the lunar orbit are captured under different viewing orientations and brightness conditions, it is necessary to normalize all images into a standard viewing geometry, which is done by setting $i=30°$, $e=0°$ and $\alpha=30°$ (Besse et al. 2013b, c; Chen et al. 2015; Hicks et al. 2011; McEwen, 1996; Yokota et al. 2011). The specific angle-set of $i=30°$, $e=0°$ and $\alpha=30°$ was adopted after lunar samples brought back from the Apollo missions were analysed at NASA's RELAB (Reflectance Experiment LABoratory) facility using these set of angles (Pieters 1983; Pieters and Hiroi 2004). Almost all lunar missions after Clementine have followed this process of standardization of lunar images with the exception of Lunar Reconnaissance Orbiter Camera (LROC) (Sato et al. 2014) which used a different set of viewing geometry (i.e., $i=60°$, $e=0°$ and $\alpha=60°$) to photometrically correct images obtained from it. An alternative process to the above mentioned standard geometries was also developed wherein the concept of equigonal albedo was used to normalize lunar data (e.g., Korokhin et al. 2018; Shkuratov et al. 1999a, b, c; Velikodsky et al. 2011, 2016). The technique of standardization of lunar images to a fixed set of viewing angles is called photometric correction or photometric normalization, which was first used with Clementine UV/VIS data (Hillier et al. 1999; Kreslavsky et al. 2000; McEwen, 1996, 1998) and later on with Chandrayaan-1 M^3 (Besse et al. 2013b, c; Hicks et al. 2011), Chang' E-1 Interference Imaging Spectrometer (IIM) (Wu et al. 2013), SELENE (Selenological and Engineering Explorer, also known as *Kaguya*) Spectral Profiler (SP) (Yokota et al. 2011), SELENE Multiband Imager (MI) (Ohtake et al. 2010), the Earth-based USGS Robotic Lunar Observatory (ROLO) (Buratti et al. 2011) and Lunar Reconnaissance Orbiter Camera Wide Angle Camera (LROC-WAC) (Sato et al. 2011, 2014). Factors such as surface topography, surface roughness, grain size and, mineral composition (Fischer et al. 1994; Fischer and Pieters 1996; McEwen 1991) influence the true surface reflectance that is generated as an output of the photometric correction and therefore these factors need to be taken into account while converting the image from radiance to reflectance.

Till date, three types of photometric corrections have been developed for lunar observations; (1) empirical (e.g., Besse et al. 2013a; Chen et al. 2015; Hicks et al. 2011; Kreslavsky et al. 2000; Wu et al. 2013; Yokota et al. 2011), (2) semi-empirical (e.g., Hillier et al. 1999; Shkuratov et al. 1999a, b, c), and (3) theoretical (e.g.,Hapke, 1963, 1966, 1993; Helfenstein and Veverka 1987; Sato et al. 2014; Shkuratov et al. 2018). A theoretical photometric correction uses physical models that can accurately describe the relationship between the properties of the surface and surface reflectance. Such corrections are usually applied when abundant data are available. For instance, (Sato et al. 2014) used Hapke

parameters on nearly 66,000 LROC-WAC images and developed a photometric correction using an innovative "tile-by-tile" approach. However, it has been seen that an empirical correction is sufficient to correct the data in most cases (Hillier et al. 1999) and reasonably good results have been obtained from them. Empirical techniques also tend to be simpler and much faster than theoretical methods (McEwen 1991). An ideal photometric correction would be performed after several observations (at least six) are made of the same location on the ground and under different spacecraft orientations in order to determine the six Hapke parameters (Hapke 1981) that are required for a physical approach at photometric normalization. Since this is not always possible, it is much more feasible to perform photometric correction on a sample site that is representative of a geologic feature of regional scale or the lunar surface on the whole (Yokota et al. 2011).

An accurate photometric correction offers the following benefits: (1) it helps to convert raw radiance images to true surface reflectance that aids in the mineral mapping of the surface, (2) it allows to seamlessly mosaic photometrically corrected adjacent, overlapping images, which can be later used to create global maps, and (3) images of a particular location observed from the orbit at a different time can be compared meaningfully.

The purpose of this study is to generate a preliminary empirical photometric function that would be used to correct radiance (PDS L1B) images obtained from the Hyper Spectral Imager (HySI) onboard Chandrayaan-1. HySI was designed to operate in the visible to near-infrared range, extending from 421 to 964 nm, which have been divided into 64 contiguous bands (Goswami and Annadurai 2009; Kiran Kumar and Chowdhury 2005b). Two HySI channels were chosen for this preliminary work, namely, 750 nm (band 38) and 950 nm (band 62). These channels were selected since they are used in the estimation of iron abundance of the lunar surface (Lucey et al. 1995, 2000; Shkuratov et al. 1999a, b, c; Wu et al. 2012). The methodology applied on this study was used on a HySI image that includes the landing site of the Apollo 17 mission (the Taurus-Littrow valley, near the south-eastern edge of Mare Serenitatis). The selection of this site allowed comparison of photometrically corrected HySI image with an M^3 image of the same location. In addition to M^3, data from Clementine UV/VIS and, SELENE MI have been used to validate the photometric model that was generated for HySI.

In the following sections, various data and methods used have been described (Sect. 2), details about the empirical model applied (Sect. 3), results of the fitting of the phase function derived from the application of the photometric function to HySI image as well as the comparison of results obtained with existing work and some general discussion (Sect. 4), followed by conclusions (Sect. 5).

2 Data used

2.1 Chandrayaan-1 Mission and Observations

HySI is one of the five Indian instruments onboard Chandrayaan-1 and was launched towards the Moon on 22nd October 2008 from the Indian spaceport, Satish Dhawan Space Centre. Chandrayaan-1 initially settled into a circular polar orbit, approximately 100 km above the lunar surface, thereby providing a spatial resolution of ~ 80 m/pixel and a swath width of ~ 20 km. From its vantage point, HySI has a nominal field of view of ~ 13°. Using this positioning arrangement above the Moon, images of various extents of the lunar surface were acquired (nearly 300 images), where most of the images were captured between ± 65°

north and south latitudes. Mission controllers had to adjust Chandrayaan-1's orbit several times due to several thermal issues that had plagued the spacecraft right after it reached the lunar orbit on 8 November 2008 (Boardman et al. 2011; Lundeen et al. 2011). Because of the numerous orbit corrections, HySI was not able to map the Moon in a planned, contiguous manner and as a consequence, the resultant images from HySI had different acquisition geometries (i.e., incidence angle, emission angle and phase angle), spatial resolutions and altitudes from the surface of the Moon (raised to ~ 200 km from the initial altitude of ~ 100 km resulting in a change of swath width from ~ 20 to ~ 40 km) (Boardman et al. 2011). Due to the several unplanned altitude corrections of Chandrayaan-1, the spatial resolution of HySI also increased to ~ 160 m/pixel.

The images captured by HySI have been divided into seven different optical periods (OP) (Besse et al. 2013b, c; Boardman et al. 2011). The first four OPs (from 18 November 2008 to 16 May 2009)—OP1A, OP1B, OP2A and OP2B—were the ones where the Moon was observed at the originally intended spatial resolution of ~ 80 m/pixel, while the remaining OPs (onwards of 20 May 2009)—OP2C1, OP2C2, and OP2C3—were the ones when the altitude of Chandrayaan-1 was raised to ~ 200 km. The latter OPs primarily contain more Global Mode (reduced spatial resolution) images as compared to the first batch of OPs where a few Target Mode (full spatial resolution) observations were made. The OPs have been summarized in Table 1. Additional details about the different OPs can be found in (Boardman et al. 2011). Communications from ground control with Chandrayaan-1 ceased on 28 August 2009, after spending 312 days (or, nearly 9 months) and more than 3400 orbits around the Moon.

2.2 HySI Data Used in This Study

In the present work, HySI Level 3 (CODMAC Level 3, NASA PDS L1B) RDR (Reduced Data Record) images have been used where the data are band separated, radiometrically calibrated, dark corrected and band-to-band registered (BBR). This data is similar to Chandrayaan-1 Moon Mineralogy Mapper (M^3) PDS L1B release 3.0, radiance data, which correspond to optical periods OP1 and OP2 (Table 1). The pixels in this data level provide lunar surface radiance (SI Units: W/(m^2 Sr μm)). The HySI images used in this study were obtained from the first optical period, OP1A (Table 2). Images obtained during this period had a comparatively better spatial resolution (since this was the initiation phase and therefore the lunar surface coverage from orbit was limited) than other optical periods due to

Table 1 Details of HySI optical periods, adapted from Besse et al. (2013a)

Optical period (OP)	Duration	Number of days	HySI spatial resolution (m/pixel)	Spacecraft altitude above Moon (km)
OP1A	18/11/2008 to 18/01/2009	62	80	100
OP1B	19/01/2009 to 14/02/2009	27	80	100
OP2A	15/04/2009 to 27/04/2009	13	80	100
OP2B	13/05/2009 to 16/05/2009	4	80	100
OP2C1	20/05/2009 to 23/06/2009	35	160	200
OP2C2	23/06/2009 to 22/07/2009	30	160	200
OP2C3	22/07/2009 to 16/08/2009	26	160	200

For more information regarding Chandrayaan-1 optical periods, please see Boardman et al. (2011)

Table 2 List of HySI and their corresponding M^3 image orbit numbers, product IDs and dates of observation

HySI image orbit	HySI Image ID	M^3 Image Orbit	M^3 Image ID	Date of observation
691	HYS_NR_20090105T060055600	669	M3G20090105T060105_V03_RDN	5th January, 2009
704	HYS_NR_20090106T073115220	710	M3G20090106T073125_V03_RDN	6th January, 2009
713	HYS_NR_20090107T011356760	722	M3G20090107T011405_V03_RDN	7th January, 2009

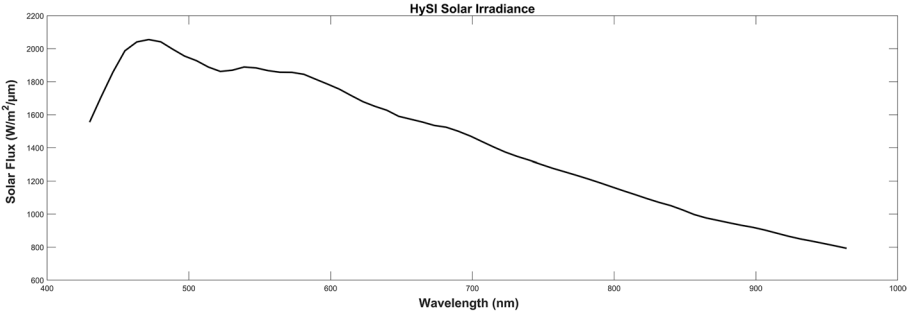

Fig. 1 HySI solar irradiance spectra plotted against wavelength that was used to generate RADF and then used for the photometric correction process

the relatively lower altitude and this was one of the factors for selecting an image from this particular OP. Additionally, the vertical swath of the particular image used for this work includes the landing site of Apollo-17 which was used for the validation of results that have been presented in further sections. The HySI RDR images were initially not referenced according to their actual surface coordinates and had to be geometrically corrected by using the image-to-image georeferencing scheme (Sect. 4), wherein an M^3 image of the same image strip as the HySI image was searched for and used in the geometric correction process. Following this, the HySI RDR radiance data (PDS L1B) was converted to reflectance (PDS L2) after the application of an empirical photometric function. The following equation (Eq. 1) was used to calculate the radiance factor (RADF; e.g., (Hapke 1993), p. 262, hereby referred to as surface reflectance) (Besse et al. 2013b; Yokota et al. 2011), using which the observed radiance was converted to apparent reflectance:

$$RADF_{\lambda}(i,e,\alpha) = \left(\frac{\left(\mathrm{I}_{\lambda}(i,e,\alpha)\right)}{J_{\lambda}} \times \pi \times R^2 \right) \tag{1}$$

where I_{λ} is the radiance of each pixel of the image, J_{λ} is the solar spectrum at a particular wavelength at 1 AU (Fig. 1), R^2 is the normalized Moon-Sun distance (derived from M^3 metadata), i is the incidence angle, e is the emission angle, and α is the solar phase angle.

Using Eq. 1, radiance values are converted to apparent surface reflectance and after a few other correction factors (mentioned in Sect. 3.1 and Eq. 2), into true surface reflectance. (Apparent reflectance derived from Eq. 1 is converted into true surface reflectance using Eq. 11 of Yokota 2011 and Eq. 2 of Besse 2013a).

2.3 Data from Other Instruments

In order to compare and validate the results obtained from HySI, data from M^3 and MI were also used in this study. Data from these instruments with comparatively higher spatial and spectral resolutions complemented HySI data. In this study, however, the usage of M^3 data was limited to the validation and comparison of the photometric function applied to HySI data as well as to georeference HySI images with respect to their corresponding M^3 images. A brief description of the other instruments is discussed in the following sub-sections and a tabular comparison highlighting the important differences between HySI and the other instruments are also presented in Table 3.

Table 3 Comparative specifications of Chandrayaan-1 HySI, Chandrayaan-1 M^3, SELENE MI, and Clementine UV/VIS instruments from which radiance and reflectance have been used in this study

Orbital parameters	Chandrayaan-1 Hyper Spectral Imager (HySI)	Chandrayaan-1 Moon Mineralogy Mapper (M^3)	SELENE (Kaguya) Multiband Imager (MI)	Clementine Ultra-Violet and Visible Camera (UV/VIS)
Spatial resolution (m/pixel)	1) 80 from 100 km altitude; 2) 160 from 200 km altitude	1) 70 from 100 km altitude (TM, target mode); 2) 140 from 100 km altitude (GM, global mode); 3) 280 from 200 km altitude (GM)	1) 20 in visible (five bands) from 100 km altitude; 2) 62 in near infrared (four bands) from 100 km altitude	100 to 200 from 425 km altitude
Swath width (km)	~20 (from 100 km altitude)	~42 (from 100 km altitude)	~19 (from 100 km altitude)	~39 (from 425 km altitude)
Field of View (Degree)	13	24	11 (Visible), 11.2 (NIR)	5.6×4.2
Spectral range (nm)	(430–964), divided into 64 contiguous bands	(460–2980), divided into 85 contiguous bands (GM) and 260 bands (TM)	(415–1550), divided into 9 non-contiguous bands	(415–1000), divided into 5 non-contiguous bands
Spectral resolution (nm)	8 to 15	20 to 40 (GM) 10 (TM)	20 (415–950), 30 (1000–1250), 50 (1550)	20 (415–750), 15 (900–1000)
Precision (SNR)	> 100 (for mature mare soil between ± 60°)	> 400 (equatorial region) > 100 (polar region)	> 100 (Visible) > 300 (Near Infrared)	> 100
Imaging mode	Push-broom	Push-broom	Push-broom	Push-broom
Quantization (bits)	12	12	10 (Visible) 12 (Near Infrared)	8
% age of the lunar surface mapped	~70%	~95%	98%	~99%

2.4 Study Area: Apollo-17 Landing Site

A region on the lunar surface was selected to study a suitable point of reference for the validation of the photometric function used here. In this regard, the Apollo-17 landing site was chosen as the testbed for this work. The Apollo-17 mission touched down at the edge of Mare Serenitatis, at the Taurus-Littrow Valley located at 20.19° N and 30.77° E (Davies and Colvin 2000; Haase et al. 2012, 2019) on 19th December 1972. The approximate location of the landing site (Fig. 2) is indicated in the centre of one of the HySI images used in this work. In addition, two more HySI images of the near vicinity were used to improve the accuracy of the photometric fit (Fig. 3). Corresponding images of the same location were also used from M^3 and MI using radiance as well as reflectance values for comparison. Samples brought back from the Moon as well as orbital studies indicate a basaltic origin

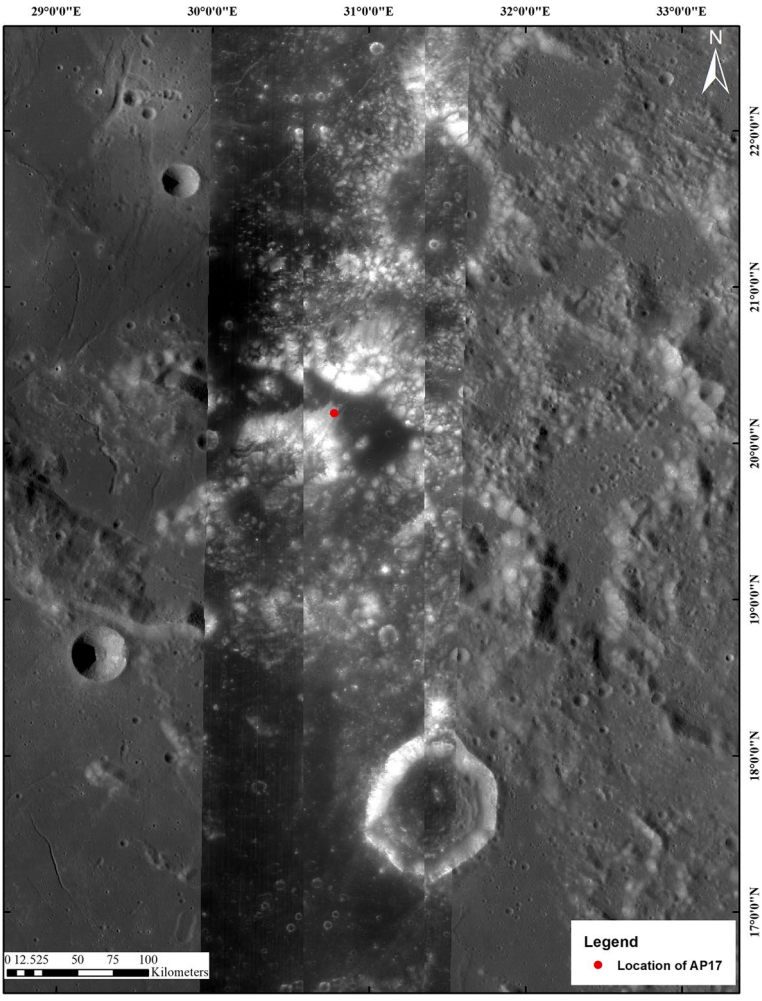

Fig. 2 The approximate landing site of the Apollo-17 mission is depicted on a HySI image overlaid on top of an LRO-WAC (Lunar Reconnaissance Orbiter—Wide Angle Camera) global mosaic

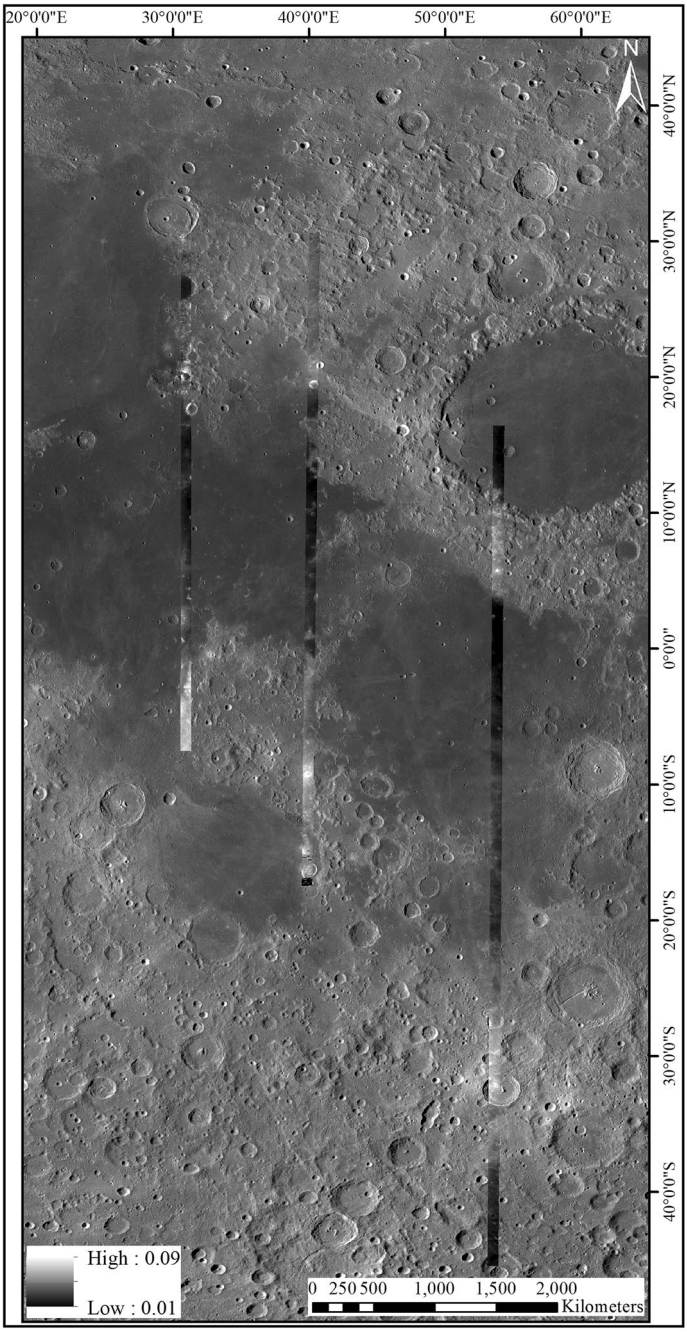

Fig. 3 Map showing the location of three of the best-quality HySI images (image orbits from the left of the image are 713, 704 and 691, respectively and the base image is a global lunar mosaic of LRO-WAC at a spatial resolution of 100 m/pixel)

for the region around the landing site (O'Hara 2001; Schmitt 1973; Schmitt et al. 2017; Wolfe et al. 1975). This could be one of the chief reasons for the relatively low reflectance values derived from HySI, M^3, and MI from the landing site. Results obtained from this region as well as the image used in this work have been discussed in-depth in Sect. 4.

3 Empirical Photometric Function used in This Study

A photometric function is used to convert the observed HySI radiance to RADF (reflectance). The derivation of RADF (also referred to as bidirectional reflectance or, BRDF e.g., Hapke 1993) from intrinsic radiance depends on a set of three angles. BRDF is, therefore, a function of three angles, also called the viewing geometry angles.

3.1 Conversion of Apparent Reflectance to True Reflectance

The standard viewing geometry of $i = 30°$, $e = 0°$ and $\alpha = 30°$ (used for lunar samples analysed at RELAB) is implemented in the photometric function used in this study. In effect, RADF_λ (i, e, α) (i.e., apparent reflectance derived from Eq. 1) is now effectively converted to RADF_λ (30°, 0°, 30°) and the image is converted to the new geometry. The first step in order to convert the sensor radiance to reflectance is to divide the observed sensor radiance by the solar irradiance (a solar spectrum that estimates the amount of solar radiation that impinges on a planetary surface at HySI wavelengths (Fig. 1) which, in this case, is obtained from modeled observations of MODTRAN4 (Gueymard 2004)). The solar distance is used as a correction factor (for the correction of HySI images and was obtained from the OBS file of the corresponding M^3 observation). Therefore, RADF_λ (30°, 0°, 30°) (Besse et al. 2013a, b; Yokota et al. 2011) can now be represented as:

$$\mathrm{RADF}_\lambda(30°, 0°, 30°) = \mathrm{RADF}_\lambda(i, e, \alpha) \times \frac{\mathrm{X_L}(30°, 0°, 30°)}{\mathrm{X_L}(i, e, \alpha)} \times \frac{\mathrm{f}_\lambda(30°)}{\mathrm{f}_\lambda(\alpha)} \tag{2}$$

where $RADF_\lambda(i,\ e,\ \alpha)$ = Observed radiance factor from HySI (apparent reflectance from Eq. 1), X_L = Limb-darkening correction and, f_λ = Phase function.

The above equation (Eq. 2) is an empirical correction factor and is used here because the nature of data is such that a theoretical photometric model that has been used in some cases (for instance, Hapke 1984; Hapke et al. 2012; Sato et al. 2014; Shkuratov et al. 1999c, 2018; Yokota et al. 2011) may not be applicable to the current dataset due to the following factors—(i) a limited coverage in photometric angles across the available HySI dataset, (ii) presence of high intrinsic noise in the data, and (iii) unavailability of complete metadata for each image (e.g., data regarding pixel-wise information which would allow one to use one of the theoretical models available in literature). This normalization is applied to the two images used in the study (750 nm and 950 nm band images). In Eq. 2, $f_\lambda(\alpha)$ is an unknown term and is derived from observations made by HySI. The phase function needs to be modeled in order to obtain a reasonably good fit. There are several methods to estimate $f_\lambda(\alpha)$, some of which are discussed below.

3.2 Empirical Photometric Models

Some of the previous studies on lunar photometry have used empirical photometric models to derive the phase function, $f(\alpha)$, e.g., (Besse et al. 2013b; Buratti et al. 2011; Hicks et al. 2011; Kreslavsky et al. 2000; Wu et al. 2013) have all used data obtained from in-flight measurements in their respective studies. In these empirical models, the phase function was obtained as a fit to a 4th order polynomial, e.g., (Besse et al. 2013b; Buratti et al. 2011; Hillier et al. 1999; Wu et al. 2013) or a 6th order polynomial (e.g., Hicks et al. 2011), depending on the nature of the data. In the case of HySI, however, a 6th order polynomial was used instead of a 4th order polynomial which was used by (Besse et al. 2013b) for M^3 images, which is shown as follows:

$$f(\alpha) = A_0 + A_1\alpha + A_2\alpha^2 + A_3\alpha^3 + A_4\alpha^4 + A_5\alpha^5 + A_6\alpha^6 \quad (3)$$

Equation 3 is similar to the polynomials used by Hillier et al. (1999), Hicks et al. (2011) and Besse et al. (2013a, b) to fit the phase function, $f(\alpha)$.

3.3 Differences Between Observed Radiance Values for HySI and M^3

The HySI and M^3 images (Table 3) used here show a considerable variation in terms of the pixel radiance values. The maximum, minimum and average pixel values for: (i) a smaller image subset from the main image and, (ii) the entire image extent have been tabulated (Table 4) for HySI_AP 17 and M^3_AP 17 values which have been derived from an image subset from the original images of HySI (HYS_NR_20090107T011356760) and M^3 (M3G20090107T011405_V03_RDN), respectively. Figure 4a–d depicts the difference between the two sensors, HySI and M^3, for the region around the landing site of Apollo-17 for the 750 nm channel, while Fig. 5a, b shows the difference in radiance values for the 950 nm channel for the same location as Fig. 4a, b. For both Figs. 4a, b and 5a, b, raw HySI and M^3 radiance images have been used. It should be noted that neither Fig. 4a nor Fig. 4b have been geometrically rectified. Separate histograms plotted for the radiance values for HySI and M^3 describe a similar curve for both but vary significantly in terms of radiance (Figs. 4c, d and 5c, d). The large differences in radiance values observed between the two images must be normalized before any analysis can be performed on the radiance data and thus photometric correction is an attempt in that direction, without the application of which inadvertent errors may be introduced in the

Table 4 Comparative analysis between radiance ($Wm^{-2}sr^{-1}um^{-1}$) values obtained from HySI and M^3 images

Wavelength (nm)	Parameter	HySI_AP17	M^3_AP17	HySI_whole image	M^3_whole image	Radiance ratio_AP17	Radiance ratio_whole image
750	Minimum	2.48	17.65	2.06	8.55	7.11	4.15
	Maximum	8.23	90.53	8.23	108.76	11.00	13.21
	Average	3.53	31.03	3.17	32.51	8.79	10.25
950	Minimum	2.00	13.06	1.05	6.30	6.53	6.00
	Maximum	4.38	63.19	5.02	69.87	14.42	13.91
	Average	2.65	22.64	2.43	23.70	8.54	9.75

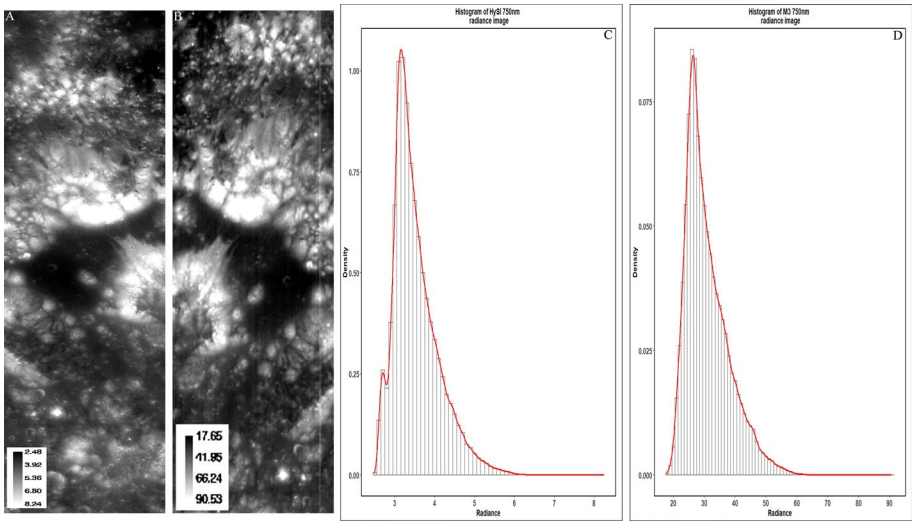

Fig. 4 **a** HySI radiance image for 750 nm and **b** M^3 radiance image for 750 nm showing the region around the Apollo—17 landing site with legends for both figures showing the image brightness scales. **c** Histograms plotted for HySI and **d** M^3 highlight the difference in radiance values of image pixels contained in (**a**) and (**b**)

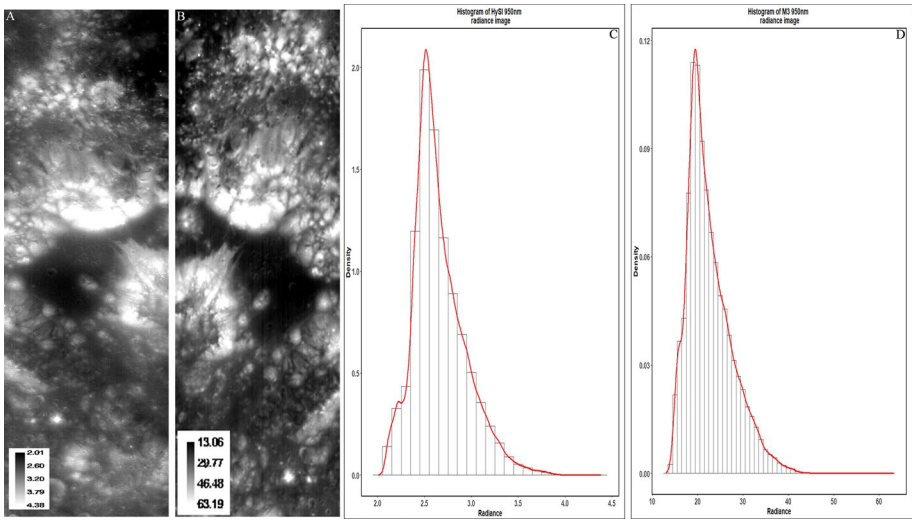

Fig. 5 **a** HySI radiance image for 950 nm and **b** M^3 radiance image for 950 nm showing the region around the Apollo—17 landing site with legends for both figures indicating the image brightness scales. **c** Histograms plotted for HySI and **d** M^3 highlight the difference in radiance values of image pixels contained in (**a**) and (**b**)

estimation of FeO/TiO_2 and other spectral analysis using spectroscopic data (Xu et al. 2020 and other references therein). A more detailed discussion highlighting the large deviation in radiance values is presented in discussions (Sects. 4.4.1 and 4.4.2) below.

3.4 Distinction Between Lunar Mare and Highland using HySI Apparent Reflectance

Some of the previous studies have clearly separated the mare region from highland regions and came up with two different photometric functions for two different lunar terrains, while others have used a common function that generally covers both regions. Helfenstein and Veverka (1987); Hillier (1999) showed that the lunar mare and highland regions have different surface properties and constituents and hence have different photometric properties.

In the case of HySI data, the approach of (Besse et al. 2013a) was followed in order to identify highland regions based on apparent reflectance (reflectance factor, REFF, and is defined as the ratio of the reflectance of a surface to that of a perfectly diffuse surface under similar illumination conditions, e.g., (Ohtake et al. 2010)). This approach was selected since it is a better approximation than SP data where only reflectance values have been used. REFF is defined by the ratio of the radiance factor and the cosine of the incidence angle ($RADF/\cos(i)$.). The three criteria that have been used to differentiate between highland and mare HySI images were formulated based on the selection criteria laid down by (Besse et al. 2013b).

1. $REFF_{748nm,max} \geq 0.02$
2. $REFF_{948nm}/REFF_{748nm} > (1.22 - 0.5 \times (REFF_{748nm}))$
3. $REFF_{948nm}/REFF_{748nm} \leq 1.25$

In our case, the first condition had to be modified in order to adjust for the much lower apparent reflectance values derived from HySI, according to radiance factor values generated by HySI data. The constraining factor used for the first condition was derived from the maximum estimated REFF among the six images that were randomly chosen after a careful visual inspection of its approximate location around the highland and mare regions. Along with the first condition, the third condition (colour ratio between 748 and 948 nm) was also modified (particular value was chosen after several iterations), keeping in line with HySI data, wherein, instead of keeping the ratio of the 948 nm and 748 nm as 1.5, it was changed to 1.25 since HySI has much lower REFF as compared to M^3. For a region to be classified as highland, all three conditions stated above must be fulfilled, otherwise, it may be classified as mare. It was found that most of the test images (four out of six) could be classified as belonging to the mare region and were satisfying the above three criteria suggesting that the correction used here can be implemented for all mare regions and some highland regions that adjoin some mare regions. Although this procedure is a crude way to identify and segregate highlands from mare regions, in our case as well as in the case of the M^3 photometric correction, it has yielded the desired results.

In this case, all three criteria were adjusted for HySI-specific data. When these criteria were applied on the image used in this study, it was found that the image could be classified as that belonging to a mare region, based on the quantitative analysis using the three criteria that were modified for HySI data. In addition, among the six images that were chosen as test images in order to estimate the HySI-specific values as well as to test the model, two images that were known to belong to the highland region were confirmed as highland images after the criteria check was applied on those images. It can, therefore, be concluded that this study deals with images that lie in a region whose surface composition could be claimed to be that of basaltic origin (Longhi et al. 1974; Snyder et al. 1994; Staid and Pieters 2001; Wentworth et al. 1979). Consequently, it could also be said that the photometric

correction presented here deals with a mare-based correction. A separate study is also necessary in order to identify specific highland regions along with good orbital coverage from Chandrayaan-1 over that region so that good quality data is available for further processing, analysis, and interpretation.

3.5 Usage of Merged LOLA-KAGUYA DEM Data

In this study, lunar topography data was made use of in order to extract surface slope and aspect, which was then used to compute pixel-level incidence and emission angles for HySI data. Topography data used in this work is obtained from the merged DEM available from LOLA and SELENE TC, with a pixel resolution of 59 m (Barker et al. 2016). The usage of merged LOLA-KAGUYA DEM allowed us to accurately extract the slope and aspect of the lunar surface. Moreover, the usage of DEM and DTM data instead of spherical assumptions has greatly improved our ability to accurately use topographic data and this improves the overall accuracy of the photometrically corrected image (Besse et al. 2013b). This is a significant improvement compared to the earlier attempts at photometric correction (e.g., (Hillier et al. 1999) for Clementine, (Yokota et al. 2011) for SELENE SP and (Mall et al. 2013) for SIR-2) which assumed the Moon to be a perfect sphere due to unavailability of global topography data at that time. Such assumptions have been known to generate large-scale discrepancies between the assumed height of sloped surfaces and their actual elevations (Robinson and Jolliff 2002). The application of lunar topography in photometric correction also helped remove the effect of topography from most of the features on the surface, which was also reported by (Besse et al. 2013a) for the photometric correction of M^3 images.

3.6 Calculation of Incidence and Emission Angles

The raw (radiance) HySI data downloaded from the ISSDC (Indian Space Science Data Centre) (https://www.issdc.gov.in/) web portal did not have the illumination geometry information in the attached HySI metadata file. Therefore, in order to perform photometric correction on a HySI image, it is essential to calculate the incidence and emission angles since these angles are directly required in the RADF and limb darkening calculations (Eq. 2). To calculate i and e, the procedure mentioned in Guo et al. (2014) was followed, wherein the Sandmeier Model (Sandmeier and Itten 1997) was applied to topographically correct M^3 data. The Sandmeier Model uses slope and aspect as the input parameters since these are indicators of the surface topography and the fact that the reflected solar radiation from the lunar surface that reaches the sensor will be determined by the surface undulations. In this study, slope and aspect of the image that was chosen for photometric correction have been derived from LOLA data that were ingested into a GIS environment, wherein the above-mentioned parameters were calculated using the Spatial Analyst in-built tool in ArcMap. Consequently, i and e (notation of i and e have been changed to prevent conflict from the notation used with slope in the equations given below) have been represented as follows:

$$i_s = \arccos\left[\cos(e)\cos(Z) + sin(e)sin(Z)\cos(\varphi_m - \varphi_s)\right] \tag{4}$$

$$i_v = \arccos\left[\cos(e)\cos(M) + sin(e)sin(M)\cos(\varphi_m - \varphi_v)\right] \quad (5)$$

where i_s = Solar incidence angle, i_v = Emission angle, Z = Solar zenith angle, M = Sensor zenith angle (Sensor elevation angle; for nadir viewing sensors, $M = 0$), e = Slope of the surface (Obtained from merged global LOLA-KAGUYA DEM), φ_m = Aspect of the surface (Obtained from merged global LOLA-KAGUYA DEM), φ_s = Solar azimuth angle and, φ_v = Sensor azimuth angle.

Some of the parameters in Eqs. 4 and 5, like φ_s, Z and,φ_v, are obtained from the Solar Parameter (SPM) file present in HySI metadata. Since pixel-wise information for HySI image is unavailable, the data (φ_s, Z,φ_v) were averaged without the application of weights and were used for the incidence and emission angle calculations.

4 Results and Discussion

In this section, the results obtained from the process of spatially transforming the HySI images have been discussed first followed by the limb darkening function used for this work, as well as the results obtained from fitting the phase function with RADF derived from HySI data. Results are also presented (in the following sub-sections) from the validation of RADF values that have been compared with reflectance values obtained from M^3 data from the landing site of the Apollo-17 mission in addition to the other locations from where images have been used (please refer Table 2 for the list of images). Additionally, the large deviation between HySI and M^3 radiance values as well as some photometric characteristics observed after performing the photometric correction of HySI have been discussed in detail. Furthermore, a brief comparative analysis between HySI and M^3 has been performed and is explained in the following sub-sections.

The raw HySI images (80 m/pixel spatial resolution) used for photometric correction were originally not georeferenced (after downloading from the ISSDC website). In order to spatially transform the images to their actual coordinates on the lunar surface, the image-to-image georeferencing process was found the most suitable for this purpose. As a result, an M^3 image (140 m/pixel spatial resolution) corresponding to each HySI image and possibly one that covers the entire vertical swath of the HySI image was selected. After a meticulous and rigorous search in the Chandrayaan-1 M^3 PDS online data archive (located at—https://ode.rsl.wustl.edu/moon/index.aspx), M^3 images were found that most closely fit the HySI image extents and were therefore selected as the reference images for the georeferencing process. Prior to using each M^3 image to co-register their corresponding HySI images, the M^3 images also needed to be geometrically rectified. This was done using the location (LOC) file available with the M^3 metadata using which a GLT (Geographic Lookup Table) file was generated in ENVI platform. Once an M^3 image was georeferenced using the GLT file, it was used as an input in order to georeference the associated HySI image. Following this, at least 25–30 common locations were chosen from across the entire swath of each M^3 image and subsequently matched on the corresponding HySI image, thereby geometrically rectifying the latter image.

Apart from the HySI image mentioned above (orbit 713), photometric correction was performed on multiple HySI images in order to test the method described in this work. The other HySI images belong to orbits 691 and 704. Corresponding M^3 image pairs (M^3 orbit 669 and M^3 orbit 710, respectively) for HySI orbits 691 and 704 were georeferenced and subsequently used to co-register the HySI images.

Once each HySI radiance image was georeferenced, the rest of the process in the radiance to reflectance conversion pipeline was followed to photometrically process the image to obtain the reflectance image, which has been discussed in the following sub-sections.

4.1 Limb Darkening Function

In this study, the Lommel-Seeliger limb darkening function has been used, which is a straightforward model that describes the lunar limb darkening. The Lommel-Seeliger function has proved to be a good model that has yielded satisfying results with M^3 as well as with Chang' E-1 IIM data (e.g., Besse et al. 2013a; Buratti et al. 2011; Hicks et al. 2011; Sato et al. 2011, 2014; Wu et al. 2013; Zhang et al. 2013)). The two functions commonly used to describe the lunar limb darkening namely, Lunar-Lambert and Lommel-Seeliger, have been compared. It was found that the Lunar-Lambert function darkened the HySI image between the phase angles of ~ 20° to ~ 48°, whereas for the same range of angles, Lommel-Seeliger was comparatively much brighter (Fig. 6b, c). In Fig. 6a–d, the results from the comparative study of the two models on HySI images is shown. When compared with some of the existing works, e.g., Besse et al. (2013a), McEwen (1996) and Yokota et al. (2011), a similar darkening at small phase angles was reported in their respective measurements while using the Lunar-Lambert model. On the other hand, Besse et al. (2013a) observed that the usage of the Lommel-Seeliger model had a relatively milder darkening on M^3 images. It was found that Lommel-Seeliger is almost twice as bright as compared to Lunar-Lambert from the HySI observations (Fig. 6d). However, this ratio quickly diminishes at higher phase angles (i.e., from ~ 1.8 at 22° to ~ 0.3 at 36°). Since the Lommel-Seeliger model does not darken the image much with respect to Lunar-Lambert, its application to HySI images is acceptable and justified.

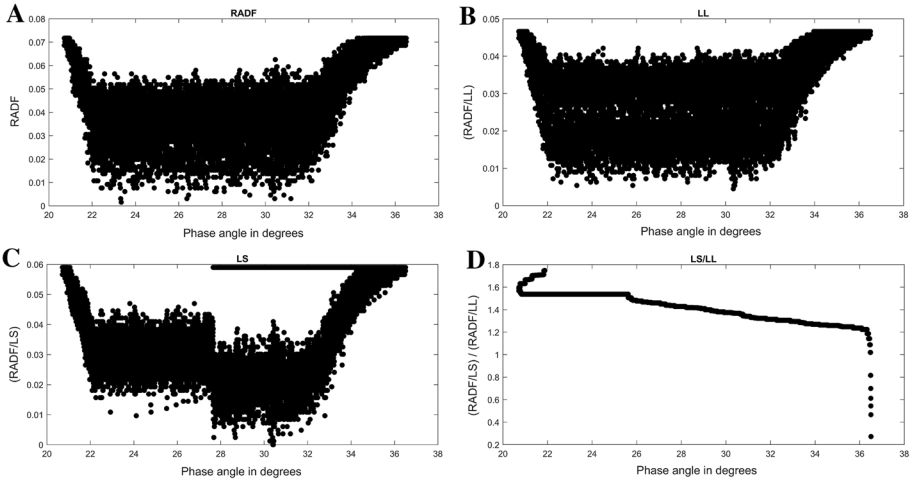

Fig. 6 Comparative plots depicting the effects of two different limb darkening functions on HySI data at 750 nm. **a** is RADF, **b** the ratio of RADF and Lunar-Lambert (RADF/LL), **c** the ratio of RADF and Lommel-Seeliger (RADF/LS) and, **d** the ratio of two functions, LL and LS

4.2 Fitting of HySI Data

In this section, the results of fitting the phase function of HySI data with a simple polynomial function have been presented. A brief discussion then follows that compares the derived $f(\alpha)$ from HySI images and $f(\alpha)$ derived from M^3, Clementine, and IIM images.

Two bands from a total of three HySI images (Orbit 691, 704 and 713) have been used to both individually as well as synergistically extract the phase function from three HySI images the $f(\alpha)$ for 748 nm (band 38, 748 nm) and 948 nm (band 62, 948 nm). In Fig. 8(a-b), $f(\alpha)$ for the two bands is shown, which uses the ratio of the radiance factor (RADF) and the Lommel-Seeliger function (LS), i.e., RADF/LS, which shows the combined phase function plot derived from all the images used in this study. $f(\alpha)$ plots were created after phase angle data was binned every 0.001°, using the binning technique applied by Besse et al. (2013a) and Yokota et al. (2011) for M^3 and SELENE SP, respectively. In Fig. 8a, the plot after binning the data is shown in red while the unbinned data is plotted in black (Fig. 8b). Data binning was necessary due to the presence of many data points (image pixels) that were derived from both the bands. The advantage of creating such bins was that the scatter of the data was constrained to a manageable amount and the corresponding polynomial fit had an excellent correlation ratio, ($R^2 \sim 0.998$) for both the bands. No weights were applied on the bins and the median values of each bin were used in the fitting process. The phase functions for both 748 nm and 948 nm exhibit a smooth trend overall and have high RADF for lower phase angles (between 18° and 25°) and low RADF for higher phase angles (between 35° and 48°). It is evident from Fig. 8 that the phase curves for the two wavelengths are largely identical and exhibit a common trend that has been described above. The only difference between Fig. 8a, b is the difference between RADF values for the two wavelengths. Radiance data from the 948 nm band was found to be very noisy while processing for this work. Due to this reason, it could be possible that the significantly low RADF/LS values for band 62 (as compared to that of M^3) are due to the presence of noise in the data and/or calibration issues resulting from the frequent altitude corrections of the Chandrayaan-1 spacecraft or could also be due to inherent instrumental errors. The sixth order polynomial used in the fitting process provided a good, smooth fit for the data from both the bands. However, (Hicks et al. 2011) chose a sixth order polynomial to fit M^3 data whereas (Besse et al. 2013a) found a fourth order polynomial to be smoother than a sixth order polynomial for their version of photometric correction of M^3 data. The results obtained from the curve fitting of HySI data reveal that except for the lower (i.e., ~ 18° to ~ 23°) and the higher (i.e., ~ 37° to ~ 48°) phase angles, the variation between the binned and unbinned fits is the least (at phase angles between ~ 24° to ~ 37°) and appears almost flat. The limited phase angle range for these images, might be the reason for the slight variation as compared with the curve-fitting plot by (Besse et al. 2013b) for the photometric correction of M^3 that can be observed in the fit. The phase function coefficients derived for HySI bands 38 and 62 (748 nm and 948 nm, respectively) as well as the associated errors obtained after fitting three HySI images of the near vicinity as referred earlier in Fig. 3 are summarised in Table 5.

In this study, the opposition surge is not accounted for since the solar phase angles at which the surge is most observed (between 0° and 4° (Buratti et al. 1996)) are not available in this particular dataset. The phase function fit obtained for HySI data in this work may only be considered for mare regions and as such, its application over highland regions may not yield expected results.

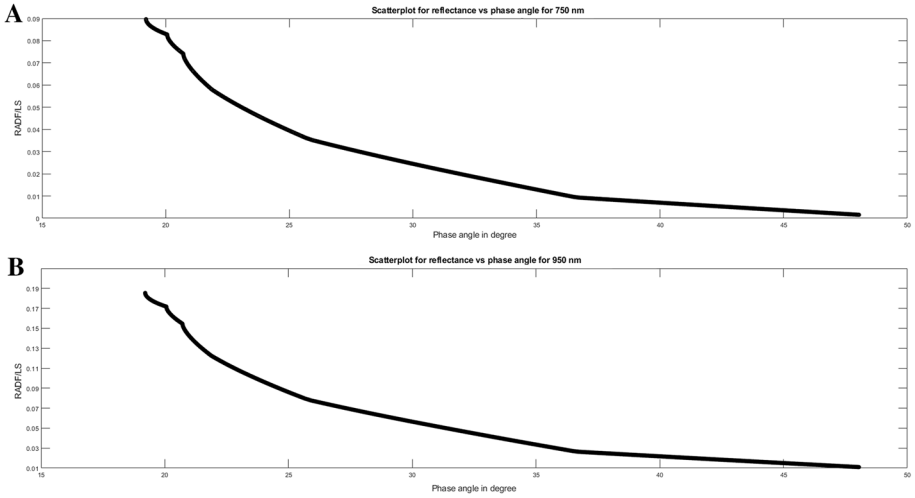

Fig. 7 Scatterplots of reflectance vs phase angle derived from multiple HySI images from OP1A for **a** 750 nm and **b** 950 nm

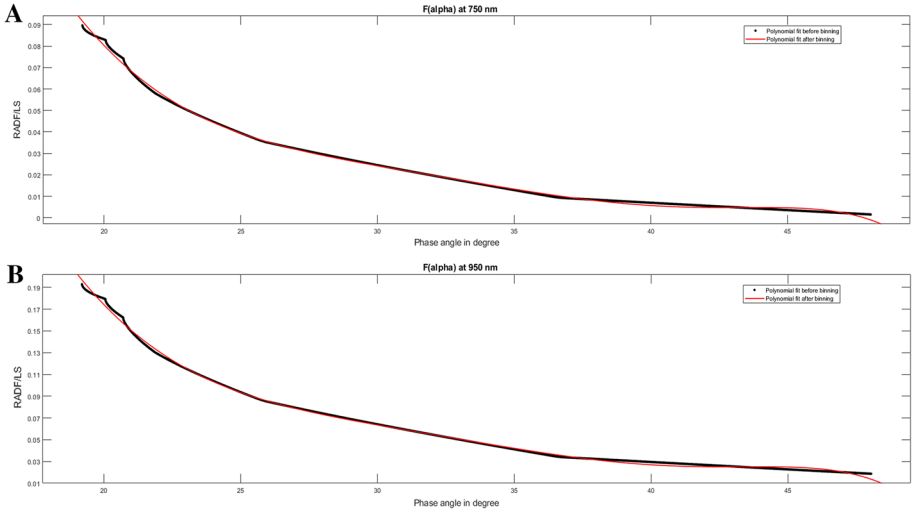

Fig. 8 Best-fit phase functions derived from multiple HySI images from OP1A for **a** 750 nm and **b** 950 nm with data adjusted for observation geometry, i.e., for incidence and emission angles, using the Lommel-Seeliger law; phase function is represented by the black curve (after data binning) and red curve (before data binning)

Table 5 Phase coefficients of HySI band 38 (748 nm) and band 62 (948 nm) derived after fitting a phase function to a sixth-order polynomial (with 95% confidence bounds)

Wavelength (nm)	A_0	A_1	A_2	A_3	A_4	A_5	A_6	SSE	R^2	RMSE
748	0.03395	− 0.0001651	0.0002466	0.003487	− 0.01171	0.0148	− 0.02348	0.118	0.998	0.001133
Errors	(0.03393, 0.03397)	(− 0.0001703, − 0.0001599)	(0.0002174, 0.0002757)	(0.003446, 0.003529)	(− 0.01176, − 0.01167)	(0.01475, 0.01486)	(− 0.02351, − 0.02345)			
948	0.08135	− 0.0004082	0.0006095	0.008621	− 0.02895	0.0366	− 0.05805	0.721	0.998	0.0028
Errors	(0.08131, 0.08139)	(− 0.0004211, − 0.0003954)	(0.0005375, 0.0006815)	(0.008518, 0.008725)	(− 0.02906, − 0.02885)	(0.03646, 0.03674)	(− 0.05812, − 0.05797)			

4.3 Validation of the Photometric Correction for HySI

The HySI images used in this work were chosen in such a way that the photometrically corrected images using the photometric function presented here could be validated with photometrically processed data from at least one more instrument (in this case, M^3), in order to check and validate the performance of the correction. One of the HySI images and its corresponding M^3 image, includes the landing site of Apollo—17 (orbit 713, Fig. 2). These and the other HySI images used in this study were carefully selected such that both the images have roughly the same time of acquisition (i.e., evening to nighttime), although incidence and emission angles were likely to vary. After comparing the average reflectance values of the Apollo—17 landing site obtained by HySI and M^3, a small variation between the reflectance values derived from the two sensors was found. For instance, at 750 nm, it was calculated that the M^3 image pixels were nearly 14% brighter than HySI for the same site (obtained from a few pixel values averaged over a small area), Possible causes for deviation from M^3—derived reflectance values have been discussed in further sub-sections.

In order to validate the photometric correction done on two bands for multiple HySI images as mentioned above, a small area centred on the landing site of the Apollo—17 mission from one of the images (orbit 713) was selected and was extracted from the main image. A visual inspection of the photometrically corrected HySI image (Fig. 9c) with respect to the image prior to the application of photometric correction (georeferenced

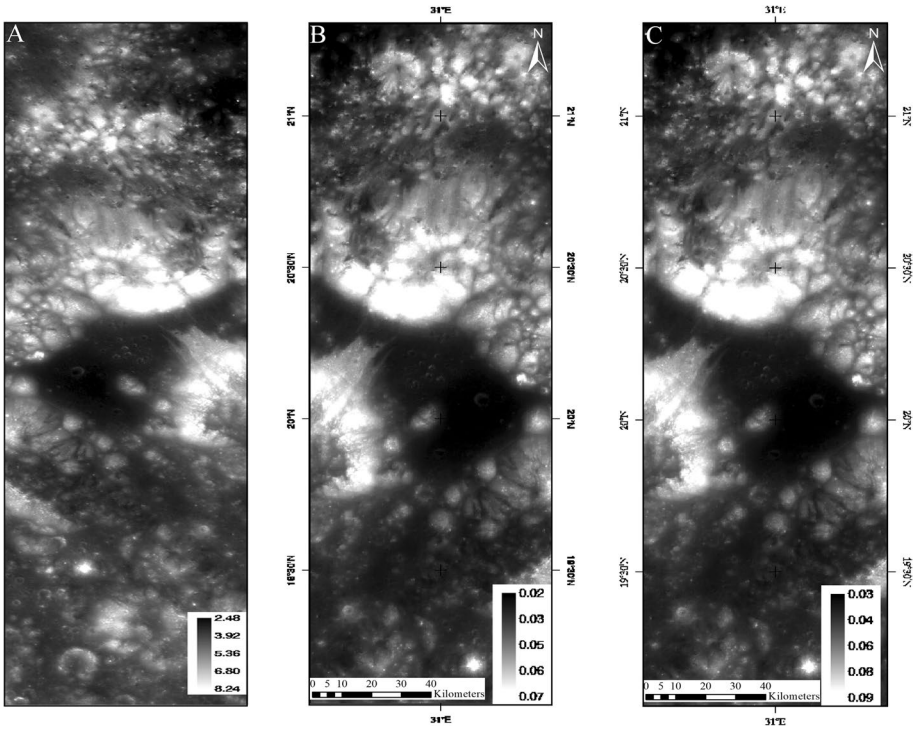

Fig. 9 **a** Comparison between the unprocessed HySI radiance image (750 nm) on the left for the Apollo—17 landing site, **b** the georeferenced apparent reflectance HySI image (750 nm) in the centre and, **c** the spatially transformed photometrically corrected HySI reflectance image (750 nm) on the right

and without photometric correction, apparent reflectance image) (Fig. 9b) reveals a few variations. After the application of photometric correction on the image shown in Fig. 9b, there is an improvement in the maximum brightness of the image, which was found to have increased by nearly 28% as compared to the geometrically corrected image (apparent reflectance image, Fig. 9b).

A scatterplot showing the relationship between reflectance (RADF/LS) and phase angle (Fig. 7(a-b)) for both channels (750 and 950 nm) displays the trend between the two parameters. Apart from the region around lower phase angles (< 26°), a relatively flatter trend can be observed for both channels in the rest of the plot (Fig. 7a, b). This correlates well with Fig. 8a, b wherein the polynomial (red) fitting the curve (black) almost overlaps with the black curve, not only signifying a good fit but also confirming the efficacy of the correction. The slight undulations visible at lower phase angles (around 20°) in Fig. 7a, b could be due to surface topography on an otherwise flat mare region from where these images have been used. In addition, there is a significant change with respect to the raw (radiance) image as well. In the raw image (e.g., Figs. 4a and 5a), some surface features (mountainsides) appear extremely bright (i.e., saturated). After the application of the photometric correction, the saturation looks to be reduced to a large extent, such that the portion depicted in Fig. 9c has a uniform brightness throughout the image, except the dark mare region in the centre of the image.

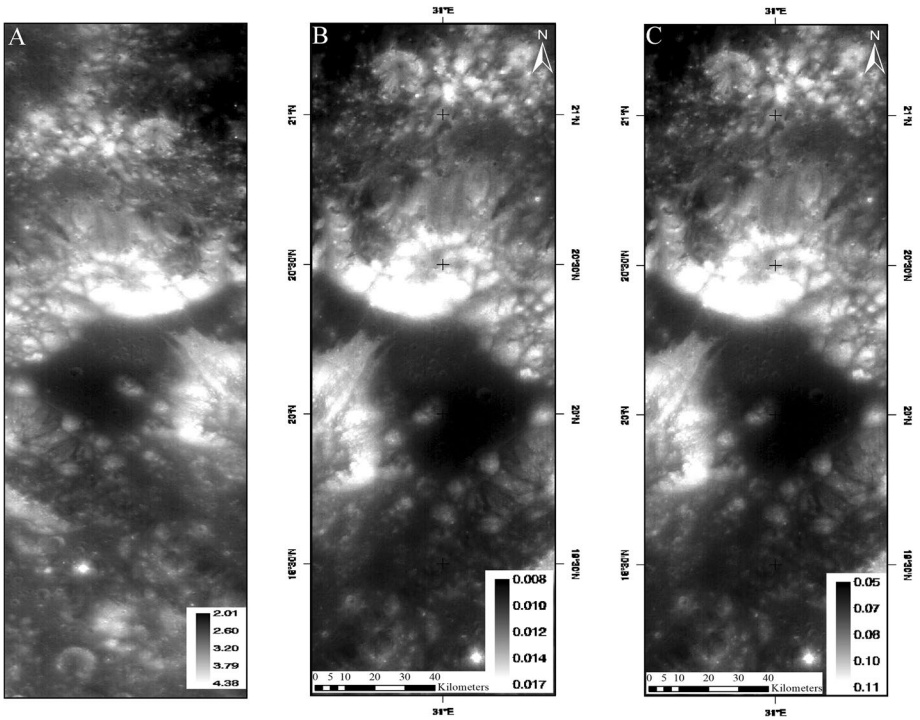

Fig. 10 **a** Comparison between the unprocessed HySI radiance image (950 nm) on the left for the Apollo—17 landing site, **b** the georeferenced apparent reflectance HySI image (950 nm) in the centre and, **c** the spatially transformed photometrically corrected HySI reflectance image (950 nm) on the right

Table 6 Comparative surface radiances and reflectances of HySI, M^3, and MI at 750 nm and 950 nm obtained from multiple images

Parameter	HySI	M^3	MI
Average pixel radiance at 750 nm (W/(m^2 Sr μm))	4.04	31.03	41.41
Average pixel radiance at 950 nm (W/(m^2 Sr μm))	3.11	22.64	31.23
Average pixel reflectance at 750 nm	0.037	0.049	0.052
Average pixel reflectance at 950 nm	0.054	0.058	0.068

Analysis done on band 62 (948 nm) also reveals similar results. In this case, the raw image (Fig. 10a) appears to have a very smooth tone throughout the image as compared to the previous image (Fig. 9a). The smoothness could be attributed to the systematic noise present in the latter bands of HySI data. In fact, the last two bands (bands 63 and 64) of HySI data contain a lot of noise to the limit of being almost unusable for any sort of image analysis or interpretation. Nevertheless, after the application of photometric correction on the raw image of band 62 (i.e., Fig. 10a), the final product appears much sharper and the brightness now seems to be more evenly distributed across the image swath (Fig. 10c). Another point to note in this case is the fact that apparent reflectance values, plotted as image brightness values on Fig. 10b, are nearly an order less as compared to the reflectance values that have been plotted as image brightness values on Fig. 10c. As previously mentioned, the raw image for band 62 possesses a lot of inherent, system-generated noise, which could have contributed to such low apparent reflectance values that have been depicted in Fig. 10b. The fact that the reflectance values have increased by nearly an order (as shown in Fig. 10c) possibly highlights the efficiency of the photometric function applied on this image as well as on the other band presented in this work (Fig. 9c).

A comparison between the 748 nm and 948 nm channels for HySI, M^3 and MI are presented in Table 6, wherein substantially higher reflectance values for HySI band 62 have been reported when compared with HySI band 38. In addition, the reflectance value for HySI bears a close resemblance with those of M^3 and MI, thereby indicating that the photometric function used here has performed well as far as data from 748 nm and 948 nm are concerned.

4.4 Discussion

4.4.1 Radiance and Reflectance Comparison of HySI and M^3 at 750 nm Channel

In this section, the differences observed between HySI and M^3 are discussed in detail, especially the quantitative aspect for both radiance and reflectance. The two images used for the comparison (M^3: M3G20090107T011405_V01_RFL and photometrically corrected HySI: HYS_NR_20090107T011356760) reveal a few differences between the results of the empirical photometric function applied on the two instruments. In general, the radiance image (PDS level 1B data) of M^3 (M^3 radiance image: M3G20090107T011405_V03_RDN) (Fig. 4b) is significantly brighter than its corresponding HySI image (Fig. 4a), mainly because the inherent surface radiance sensed by M^3 was much more than that of HySI. As per the data given in Table 4, on an average, radiance of HySI and M^3 (for 750 nm) varies by a factor of ~ 9 (i.e., the ratio between the radiance of M^3 to that of HySI, hereafter referred to as the radiance ratio) for the small image subset (Fig. 4a, b)

that includes the landing site of Apollo—17. In addition, the radiance ratio for the cropped image varies between a factor of ~ 7 and ~ 11. On the other hand, if the entire image extent is taken into consideration, on an average, the radiance ratio for the two instruments varies by a factor of ~ 10 (for 750 nm). In fact, the difference between the maximum radiance (value) for the two sensors in the given images is ~ 100 $Wm^{-2}sr^{-1}$(units of radiance referred to as SI units hereafter) (i.e., $Radiance_{MaxM^3\_Whole\ image}$–$Radiance_{MaxHySI\_Whole\ image}$ = ~ 100 SI units), while the minimum radiance (in values) has a relatively lesser variation (~ 6.5 SI units), obtained using ENVI software. The large difference that was observed between the two instruments can be highlighted by the fact that the maximum radiance for HySI (for the entire image) is ~ 8.23 SI units which is equivalent to the minimum radiance for M^3 (for the entire image) is ~ 8.55 SI units. On the other hand, the average reflectances at the Apollo—17 landing site for HySI and M^3 are ~ 0.037 and ~ 0.049 respectively (Table 6). Furthermore, the difference in reflectance values may be attributed to the fact that the observed radiance of the two images at the Apollo—17 landing site are drastically different, which in this case are ~ 4 SI units for HySI and ~ 31 SI units for M^3. However, in spite of the large difference in radiance values observed between HySI and M^3, it can be clearly seen that the effect of different radiance values has been normalized to a great extent along with the elimination of the impact of viewing geometry and illumination effects after the application of photometric correction on HySI where the average reflectance of the 750 nm and 950 nm channels are nearly equivalent to M^3 as well as to MI. Table 7 shows comparative maximum, minimum and average reflectances of HySI, M^3, and MI at 750 and 950 nm for the entire image extent covered by all these images used in this study corresponding to the landing site of Apollo—17.

Substantially higher values of radiance observed for M^3 as compared to HySI have therefore prompted us to investigate the possible reasons behind such a large difference since both the sensors are placed on the same observation platform. Some plausible reasons behind the large, noticeable variation between the radiance values obtained for the two instruments on the same spacecraft to the Moon are discussed here. One of the possible reasons behind such deviation between M^3 and HySI radiance values could be the fact that the incidence and emission angles of the two instruments on the surface are different over the same location. Average incidence angles over the Apollo—17 landing site for M^3 are ~ 30°, while the emission angles over the same location for M^3 are ~ 2° (obtained from the M^3 observation file (OBS) of the reference image). On the other hand, incidence and emission angles for the entire M^3 image vary between ~ 20° to ~ 37° and ~ 0.2° to ~ 13°, respectively. Meanwhile, the calculated incidence and emission angles (procedure for calculation in Sect. 3.6) for the entire HySI image are ~ 63° and ~ 8°, respectively. The considerably lower incidence angle range for M^3 may influence the radiance measured which is significantly higher than that of HySI owing to a considerably larger incidence angle

Table 7 Comparative maximum, minimum and average reflectances of HySI, M3, and MI at 750 and 950 nm for the entire image extent corresponding to the landing site of Apollo—17

Parameter	HySI	M^3	MI
Reflectance at 748 nm *750 nm for M^3 and MI	Max: 0.09 Min: 0.015 Avg: 0.037	Max: 0.22 Min: 0.02 Avg: 0.07	Max: 0.25 Min: 0 Avg: 0.052
Reflectance at 948 nm *950 nm for M^3 and MI	Max: 0.13 Min: 0 Avg: 0.058	Max: 0.26 Min: 0.02 Avg: 0.08	Max: 0.26 Min: 0 Avg: 0.068

Table 8 Comparison between some sensor-specific parameters for M^3 (orbit 654) and HySI (orbit 691)

Parameter	M^3			HySI		
Sensor type	Imaging spectrometer (two-dimensional HgCdTe array detector)			Active Pixel Sensor (CMOS sensor)		
Product ID	M3G20090105T060105_V03_RDN			HYS_NR_20090105T060055600		
Orbit number	654			691		
Date of observation	2009-01-05T06:01:05.000			2009-01-05T06:00:55.600		
Parameter	**Max**	**Min**	**Mean**	**Max**	**Min**	**Mean**
Solar azimuth	131	25.36	65.62	130.81	26.6	66
Solar zenith	47.94	18.45	27.95	48.05	19.11	24.55
Sensor zenith	13	0.35	6.32	NA	NA	NA
Phase	53.25	7.02	27.81	48.04	19.2	28.05
Sensor radiance	106.3	4.58	36.32	10	2.43	4.25

for HySI. Pieters et al. (2013) have stated that MI and the earth based ROLO images were acquired at relatively smaller solar incidence angles as well as phase angles and are comparatively brighter as compared to the other instruments discussed therein.

Furthermore, in order to understand likely causes behind the difference between radiance measured by the two sensors, we also compared Sun parameter and sensor parameters (along with other parameters) for both M^3 and HySI images for the same orbit and same observation date obtained from the respective sensor metadata. It is well known that CCD detectors such as the two-dimensional HgCdTe array detector used by M^3 (Green et al. 2011) produce relatively higher quality images at comparatively higher resolutions whereas CMOS sensors such as the Active Pixel Sensor (APS) with which HySI is equipped (Kiran Kumar et al. 2009b) are superior to CCD sensors in terms of power consumption, smaller size and low cost (Bigas et al. 2006; Wang and Lin 2012). From the data given in Table 8, it is evident that most of the parameters for M^3 closely correspond to HySI. However, the sensor zenith for HySI was not available with its metadata which could possibly be the reason for any variation in sensor radiance value ranges (maximum-minimum) of these sensors which has been mentioned as "NA" in the table.

Considering all the possible causes mentioned above with respect to an observed difference in radiance values estimated by these two sensors, viz., (a) difference between incidence and emission angles of the two instruments, (b) possible variation between sensor zenith and, (c) difference in sensor optics of the two sensors. Therefore, a combination of the above possible reasons might have an impact on the radiance values sensed by M^3 and HySI. However, after the application of photometric correction on the HySI images used, most of these effects such as incidence angle, emission angle, phase angle, surface radiance, topography etc., have now been normalized and hence, the mean reflectance values of HySI for both 750 nm and 950 nm channels are similar to that of M^3.

4.4.2 Radiance and Reflectance Comparison of HySI and M^3 at 950 nm Channel

In this section, a quantitative discussion and comparison of the reflectance values obtained from HySI (band 62) and M^3 (band 19) at 950 nm is presented. In this case, the same set of HySI and M^3 images were used, as in the previous case, (Sect. 4.4.1). A few notable differences were observed between the photometrically corrected HySI reflectance image

and M^3 reflectance image of the same location and wavelength. Similar to the discussion of the previous section, it is also necessary to discuss the surface radiance values of this band since reflectances are derived after converting the radiance values of the images being used here. In the following parts of this section, the causes behind (i) the difference in radiance between HySI and M^3 and, (ii) the increased reflectance value for 950 nm with respect to reflectance at 750 nm, have been explained.

First of all, an attempt is made to explain the variation observed between the radiance of the two instruments, HySI and M^3. For the radiance values at 950 nm, a similar trend with respect to 750 nm can be observed with respect to a large variation between HySI and M^3 radiances. For instance, at 950 nm (for the entire image), the maximum radiance for M^3 is ~ 63 SI units, compared to just ~ 4 SI units for HySI. Therefore, although a difference of ~ 59 SI units is relatively less than the previous case, it is still high. A study by (Pieters et al. 2013) compared calibrated radiances of M^3, SELENE SP, SELENE MI and ROLO. Except for SELENE MI, the maximum difference between radiance values did not exceed 50 SI units. In (Pieters et al. 2013), radiance values for M^3 were obtained from images where mean phase angles > 45°, while in this case, mean phase angles for HySI and M^3 are ~ 24° and ~ 26°, respectively. Nevertheless, the expected difference between radiance values should not be as high as found in this case.

The maximum reflectance observed for the entire M^3 image at 950 nm is ~ 0.26 with an image-wide average of ~ 0.08. On the other hand, the maximum reflectance derived after applying the photometric correction on the corresponding HySI image is ~ 0.13 (for the entire image), with an image-wide average reflectance of ~ 0.058. Although HySI's maximum reflectance at 950 nm is half as compared to M^3, the important thing to note here is that the (maximum) reflectance of HySI is nearly 44% more than at 750 nm. Although this is a known fact that lunar reflectance spectra are red and reddening increases with phase angle (Lundeen et al. 2011), the correction applied here can be validated using this fact since expected results have been achieved in case of HySI as far as reflectance values are concerned. In addition, mean reflectance values at 950 nm for HySI (values derived from multiple images) are 0.054 compared to 0.058 for M^3. For 750 nm as well as for 950 nm, the difference between reflectance values for HySI and M^3 is quite narrow, signifying that the correction has worked well to a large extent.

Apart from the possible reasons for significantly lower sensor radiance and slightly lower mean reflectance values derived for HySI as compared to M^3, a few more probable causes are enlisted below which could be the reason for the estimation of slightly lower mean reflectance values for HySI. The photometric model applied for M^3 was optimized for the lunar highland regions (Besse et al. 2013b). Therefore, its application on a mare region (like Mare Serenitatis and parts of Mare Crisium, in this case) might be contributing to the lesser than expected reflectance values for M^3 as well as HySI. Another possible cause could be attributed to the wide range of phase angles observed for M^3 data at Mare Serenitatis. Phase angles for M^3 at Mare Serenitatis range between ~ 8° to ~ 44°, with a mean phase angle of ~ 26°. On the other hand, the mean phase angle for HySI for the same region was found to be ~ 24°. Yet another contributing factor for dissimilar reflectance values could be spatial resolution. A spatial resolution difference of ~ 60 m/pixel between HySI and M^3 could exclude several finer surface features, for example, shadows generated by surface roughness at different scales, small fresh craters, small boulders and rocks (Ohtake et al. 2013) might influence the overall reflectance of any sensor. In this case, HySI has an advantage over M^3 since it has a better spatial resolution which should aid in better interpretation of the underlying geology and surface composition through spectral analysis. Finally, the reflectance ($RADF_\lambda$)

from HySI as well as M^3 is controlled by the phase function coefficients (derived empirically) obtained from the fitting of the phase function of 750 nm and 950 nm HySI data. Since reflectance is directly calculated from $f(\alpha)$, the final $RADF_\lambda$ is dependent upon the phase function coefficients. It is important to mention that systematic photometric effects, as well as possible instrumental artifacts, could have a role to play in the calculation and the observed difference of reflectance between HySI and M^3. Since this study deals with images captured from the lunar maria, a more comprehensive study that analyses these photometric parameters across a larger set of wavelengths and regions (i.e., highlands) is beyond the current scope of the study, and therefore, it is necessary to perform further studies in this domain with HySI data in order to properly address these issues more clearly.

4.5 HySI-Derived Phase Function and Comparison with Phase Functions of M^3 and Clementine

A comparative study of the phase functions obtained from the fitting of reflectance and phase angle can be a good way to interpret the differences between the various photometric models applied to different instruments (Besse et al. 2013c). In this section, a comparison between the phase functions obtained from M^3 and Clementine UV/VIS with HySI for 750 nm and 950 nm has been attempted.

4.5.1 Comparison of the HySI-Derived Phase Function with M^3 at 750 nm

In order to compare the phase function derived for HySI with that of M^3, data from (Besse et al. 2013b) and (Hicks et al. 2011) was used as the reference data. Phase functions for M^3 were initially derived by Hicks et al. (2011) for "mare" and "not-mare" (highland) regions, with a limited amount of data. However, the derived M^3 phase function was applicable only for a fixed (24 to 90 degrees) phase angle range (Hicks et al. 2011). An improvement on this was achieved by Besse et al. (2013a), wherein data from OP2C1 (0–90 degrees) was used instead of OP1B (35–90 degrees) and OP2A (40–90 degrees) that allowed a much larger range of phase angles. In addition, it was also observed that at smaller phase angles ($<40°$), the differences between the phase functions derived from other instruments like SP, ROLO, UV/VIS and the phase function for M^3 obtained by (Hicks et al. 2011) could exceed the more recently derived phase function for M^3 by ~ 50% (Besse et al. 2013a).

In particular, when the M^3 phase function at 750 nm (Besse et al. 2013b) is compared with that of HySI at 750 nm (Fig. 8a, present study), two important features of the plot are clearly visible. First, the (absolute) reflectance (i.e., RADF/LS) of HySI is one order less as compared to M^3, although the mean reflectances are much similar. This is also mentioned in Sect. 4.4.1, wherein possible reasons for the differences between the reflectances of HySI and M^3 have been discussed in detail. Secondly, the overall trend of the fitted polynomial derived from the phase function fit of HySI is largely similar to that of M^3. This is not surprising since the image acquisition geometry of HySI and M^3 is nearly the same and particular care was taken in order to select images of the same area as well as with nearly identical acquisition time. In addition, this also verifies the accuracy and applicability of the current photometric correction on HySI data. A good fit ($R^2 = 0.998$) was achieved between phase angle and reflectance since reflectances (RADF/LS) obtained from HySI

were binned every 0.001°, which allowed the polynomial function to properly adjust itself with respect to the reflectance values and generate a good correlation.

4.5.2 Comparison Between the HySI-Derived Phase Function with Clementine UV/VIS at 750 nm

In order to verify and validate the photometric function used for HySI demonstrated in this study, the phase function of HySI was compared with that of Clementine UV/VIS for 750 nm. Several studies in the past have derived the phase function for Clementine (Buratti et al. 1996; Hillier et al. 1999; Kreslavsky et al. 2000; Shkuratov et al. 1999c) but most of these phase functions were fit with normalized reflectance, instead of the sensor-derived reflectance. Since normalized reflectance is not being used to fit the data in this study, the phase function derived by (Hillier et al. 1999) was chosen for comparison. This particular phase function was obtained empirically as well as through theoretical models. In this case, the phase function derived from the UV/VIS 'B' filter (i.e., 750 nm) was compared with HySI.

In the case of HySI data, the trend of the phase curve, with respect to Clementine for the lunar maria is replicated; the major difference being the plot for 'B' filter of UV/VIS which returned much higher reflectance as compared with HySI. In addition, phase curves for the highland regions suggest a similar pattern, wherein a maximum reflectance of ~ 0.6 was observed for the 'B' filter (at $\alpha = 0°$). On the other hand, the HySI-derived phase function for 750 nm has a slightly wavy appearance and indicates a relatively brighter surface at lower phase angles (20°–24°) compared to phase angles > ~ 30°. One of the possible causes for the wavy nature of the HySI phase curve at 750 nm could be the fact that, when compared to M^3 where pixel-level information (e.g., incidence and emission) is available, whereas the same is not available for HySI and consequently due to the fact that incidence and emission angles for HySI had to be derived using the merged LOLA-KAGUYA DEM data and by following the procedure to calculate incidence and emission angles by Guo et al. (2014), some inadvertent errors or over/under-estimations of certain parameters might have had crept in during the estimations. Therefore, due to the approximations which were necessary in order to carry out the photometric correction for HySI, the derived phase curves exhibit a wavy fit, which is largely unseen with M^3, UV/VIS or SP data. An in-depth study regarding the photometric correction of HySI data in future could reveal the actual reasons behind this.

5 Conclusions

Photometric correction of lunar images in the visible to near-infrared range is required in order to normalize the images that are acquired at different observational angles into a standard viewing geometry, in this case, $i = \alpha = 30°$, and $e = 0°$. A photometric correction for HySI-derived visible and near-infrared images has been empirically derived. One of the purposes of this photometric correction is to convert radiance data (HySI level 3, NASA PDS level 1B) to true surface reflectance (NASA PDS level 2A), which would allow generation of reflectance-based image mosaics as well as the derivation of spectral profiles over the lunar surface. Lunar topography (merged LOLA-KAGUYA DEM at 59 m/pixel)

was used to estimate incidence and emission angles which were ultimately used in the correction procedure.

M^3 (PDS level 1 and 2) data were used in this study to both compare as well as validate with photometrically corrected HySI data. Upon comparison, it was found that the M^3-observed radiance, as well as the derived surface reflectance image of the same area (i.e., similar image pixels over the same surface) as viewed by HySI, was much brighter as compared to HySI. An attempt was made to understand the reasons behind the observed difference in radiances. After a thorough analysis of the metadata of both M^3 and HySI, it was found that the variation in radiance values observed by these two sensors were due to factors such as difference between incidence and emission angles of the two instruments, possible variation between sensor zenith angles and difference in type of optics used for the two sensors. Regardless of the difference between radiance values estimated by the two sensors, the mean surface reflectance obtained for HySI post application of photometric correction on the radiance image of HySI was found to be nearly the same as compared to the mean surface reflectance of M^3 for all the images used in this study.

Results from HySI were also compared with reflectances estimated from SELENE MI at 750 nm. Images with two different spatial resolutions were used to study the reflectance and compare with that of HySI. Overall, the MI image was the brightest of the lot, followed by M^3 and HySI. This could be directly related to the low level of radiance measured by HySI. In addition, the photometric correction of MI was done using a DEM generated by MI data. Since a comparison is being made for two different instruments whose topographic correction was done using different sets of elevation data, it is likely that a different result would be obtained as far as reflectance is concerned.

Lastly, phase functions were derived for the two bands of HySI data (750 nm and 950 nm). Although the HySI phase angles were restricted between ~ 20° and ~ 48°, similarities with the M^3-derived phase functions were observed in the trend of the plots of the phase functions. HySI-derived phase functions were also compared with Clementine UV/VIS camera, wherein the trend of the plot derived from the 'B' filter (750 nm) as well as the 'D' filter (950 nm) was largely replicated, with the only exception being comparatively lower reflectance derived for HySI as compared to UV/VIS. The phase function plot of HySI has a wavy nature for both 750 nm and 950 nm possibly due to non-availability of complete metadata for HySI. Furthermore, the corrections achieved for HySI can also be useful for Imaging Infra-Red Spectrometer (IIRS) onboard Chandrayaan-2.

Acknowledgements We acknowledge the use of data from Chandrayaan-1, the first lunar mission of Indian Space Research Organization (ISRO), archived at the Indian Space Science Data Centre (ISSDC). Financial support for this work under Chandrayaan-1 Announcement of Opportunity (AO) project from Space Applications Centre, Indian Space Research Organization, Department of Space, Government of India is also acknowledged. We also thank the M^3 science team at Brown University and NASA JPL for providing processed L1B and L2A data. The LRO-LOLA team is thanked for providing global lunar DEM through the USGS Astrogeology Science Center. We thank the SELENE (KAGUYA) MI team and the SELENE Data Archive for providing the SELENE (KAGUYA) data. SELENE is a Japanese mission developed and operated by JAXA. SELENE MI team is also thanked for the provision of a global mosaic of 750 nm reflectance data in the USGS Astrogeology Center. Raja Biswas is thanked for helping with geometric rectification of HySI images and general discussion.

Author's Contributions Conceptualization: Subhadyouti Bose, Mili Ghosh Nee Lala and Akhouri Pramod Krishna. Methodology: Subhadyouti Bose and Mili Ghosh Nee Lala. Formal analysis and investigation: Subhadyouti Bose. Data curation and software: Subhadyouti Bose. Writing – original draft preparation: Subhadyouti Bose. Writing – review and editing: Subhadyouti Bose, Mili Ghosh Nee Lala and Akhouri Pramod Krishna. Funding acquisition: Mili Ghosh Nee Lala and Akhouri Pramod Krishna. Resources: Mili

Ghosh Nee Lala and Akhouri Pramod Krishna. Supervision: Mili Ghosh Nee Lala and Akhouri Pramod Krishna.

Funding Financial support through a project grant under an Announcement of Opportunity (AO) for Chandrayaan-1 data from the Space Applications Centre, Indian Space Research Organization, Department of Space, Government of India is gratefully acknowledged.

Availability of Data and Material All data used in this work is freely available online in the respective portals of the instruments, i.e., Chandrayaan-1 HySI and M^3, merged LOLA-KAGUYA DEM, SELENE SP and Clementine UV/VIS camera.Code Availability All code (MATLAB and R) used in this work is freely available online.

Declaration

Conflict of interest The authors declare that they have no conflict of interest.

References

A.S. Arya, R.P. Rajasekhar, K. Sur, B. Gopala Krishna, K. Suresh, T.P. Srinivasan, K.V. Iyer, P. Chauhan, A.S. Ajai Kiran Kumar, A.D. Pandey, A. Khare, P.K. Verma, Morphometric and rheological study of lunar domes of Marius Hills volcanic complex region using Chandrayaan-1 and recent datasets. J. Earth Syst. Sci. **127**, 70 (2018). https://doi.org/10.1007/s12040-018-0971-y

M.K. Barker, E. Mazarico, G.A. Neumann, M.T. Zuber, J. Haruyama, D.E. Smith, A new lunar digital elevation model from the Lunar Orbiter Laser Altimeter and SELENE Terrain Camera. Icarus **273**, 346–355 (2016)

S. Besse, P.J. Isaacson, T. Matsunaga, J.M. Sunshine, M. Ohtake, J.W. Boardman, Y. Yokota, C.M. Pieters, S. Yamamoto, U. Mall, R.O. Green, J. Haruyama, M.I. Staid, One Moon, many measurements 1: radiance values. Icarus **226**, 951–963 (2013a). https://doi.org/10.1016/j.icarus.2013.07.008

S. Besse, J. Sunshine, M. Staid, J. Boardman, C. Pieters, P. Guasqui, E. Malaret, S. McLaughlin, Y. Yokota, J.Y. Li, A visible and near-infrared photometric correction for Moon Mineralogy Mapper (M3). Icarus **222**, 229–242 (2013b). https://doi.org/10.1016/j.icarus.2012.10.036

S. Besse, Y. Yokota, J. Boardman, R. Green, J. Haruyama, P. Isaacson, U. Mall, T. Matsunaga, M. Ohtake, C. Pieters, M. Staid, J. Sunshine, S. Yamamoto, One Moon, many measurements 2: photometric corrections. Icarus **226**, 127–139 (2013c). https://doi.org/10.1016/j.icarus.2013.05.009

S. Bhattacharya, P. Chauhan, A.S. Rajawat, A.S.K. Ajai Kumar, Lithological mapping of central part of Mare Moscoviense using Chandrayaan-1 Hyperspectral Imager (HySI) data. Icarus **212**, 470–479 (2011). https://doi.org/10.1016/j.icarus.2011.02.006

S. Bhattacharya, D. Lal, M. Chauhan, P. Chauhan, A.S. Ajai Kiran Kumar, Detection of hydroxyl-bearing exposures of possible magmatic origin on the central peak of crater Theophilus using Chandrayaan-1 Moon Mineralogy Mapper (M3) data. Icarus **260**, 167–173 (2015). https://doi.org/10.1016/j.icarus.2015.07.013

S. Bhattacharya, S. Saran, A. Dagar, P. Chauhan, M. Chauhan, A. Ajai, S.K. Kumar, Endogenic water on the Moon associated with non-mare silicic volcanism: implications for hydrated lunar interior. Curr. Sci. **105**, 685–691 (2013)

M. Bigas, E. Cabruja, J. Forest, J. Salvi, Review of CMOS image sensors. Microelectronics J. **37**, 433–451 (2006). https://doi.org/10.1016/j.mejo.2005.07.002

J.W. Boardman, C.M. Pieters, R.O. Green, S.R. Lundeen, P. Varanasi, J. Nettles, N. Petro, P. Isaacson, S. Besse, L.A. Taylor, Measuring moonlight: an overview of the spatial properties, lunar coverage, selenolocation, and related Level 1B products of the Moon Mineralogy Mapper. J. Geophys. Res. E Planets **116**, 1–15 (2011). https://doi.org/10.1029/2010JE003730

B.J. Buratti, M.D. Hicks, J. Nettles, M. Staid, C.M. Pieters, J. Sunshine, J. Boardman, T.C. Stone, A wavelength-dependent visible and infrared spectrophotometric function for the Moon based on ROLO data. J. Geophys. Res. E Planets **116**, 1–8 (2011). https://doi.org/10.1029/2010JE003724

B.J. Buratti, J.K. Hillier, M. Wang, The lunar opposition surge: observations by clementine. Icarus **124**, 490–499 (1996). https://doi.org/10.1006/icar.1996.0225

L.C. Cheek, C.M. Pieters, J.W. Boardman, R.N. Clark, J.P. Combe, J.W. Head, P.J. Isaacson, T.B. McCord, D. Moriarty, J.W. Nettles, N.E. Petro, J.M. Sunshine, L.A. Taylor, Goldschmidt crater and the Moon's

north polar region: results from the Moon Mineralogy Mapper (M3). J. Geophys. Res. E Planets **116**, 1–15 (2011). https://doi.org/10.1029/2010JE003702

C. Chen, C. Zhang, A. Ghulam, Q. Qin, L. Chen, W. Fa, H. Zheng, Photometric correction and reflectance calculation for lunar images from the Chang'E-1 CCD stereo camera. J. Opt. Soc. Am. A **32**, 2409 (2015). https://doi.org/10.1364/josaa.32.002409

M.E. Davies, T.R. Colvin, Lunar coordinates in the regions of the Apollo landers. J. Geophys. Res. Planets **105**, 20277–20280 (2000). https://doi.org/10.1029/1999JE001165

E.M. Fischer, C.M. Pieters, Composition and exposure age of the Apollo 16 Cayley and Descartes regions from Clementine data: normalizing the optical effects of space weathering. J. Geophys. Res. Planets **101**, 2225–2234 (1996)

E.M. Fischer, C.M. Pieters, S.F. Pratt, Modeling the space weathering-induced optical alteration of lunar soils: first results. in Lunar and Planetary Science Conference. p. 371 (1994)

J.N. Goswami, M. Annadurai, Chandrayaan-1: India's first planetary science mission to the moon. Curr. Sci. **96**, 486–491 (2009)

R.O. Green, C. Pieters, P. Mouroulis, M. Eastwood, J. Boardman, T. Glavich, P. Isaacson, M. Annadurai, S. Besse, D. Barr, B. Buratti, D. Cate, A. Chatterjee, R. Clark, L. Cheek, J. Combe, D. Dhingra, V. Essandoh, S. Geier, J.N. Goswami, R. Green, V. Haemmerle, J. Head, L. Hovland, S. Hyman, R. Klima, T. Koch, G. Kramer, A.S.K. Kumar, K. Lee, S. Lundeen, E. Malaret, T. McCord, S. McLaughlin, J. Mustard, J. Nettles, N. Petro, K. Plourde, C. Racho, J. Rodriquez, C. Runyon, G. Sellar, C. Smith, H. Sobel, M. Staid, J. Sunshine, L. Taylor, K. Thaisen, S. Tompkins, H. Tseng, G. Vane, P. Varanasi, M. White, D. Wilson, The Moon Mineralogy Mapper (M3) imaging spectrometer for lunar science: Instrument description, calibration, on-orbit measurements, science data calibration and on-orbit validation. J. Geophys. Res. Planets (2011). https://doi.org/10.1029/2011JE003797

C.A. Gueymard, The sun's total and spectral irradiance for solar energy applications and solar radiation models. Sol. Energy **76**, 423–453 (2004). https://doi.org/10.1016/j.solener.2003.08.039

P. Guo, S. Chen, J. Wang, Y. Lian, M. Ma, Y. Li, Lunar clinopyroxene abundance retrieved from M3 data based on topographic correction. Planet. Geod. Remote Sens. **157** (2014)

I. Haase, J. Oberst, F. Scholten, M. Wählisch, P. Gläser, I. Karachevtseva, M.S. Robinson, Mapping the apollo 17 landing site area based on Lunar Reconnaissance Orbiter Camera images and Apollo surface photography. J. Geophys. Res. Planets **117**, E00H20 (2012). https://doi.org/10.1029/2011JE003908

I. Haase, M. Wählisch, P. Gläser, J. Oberst, M.S. Robinson, Coordinates and maps of the apollo 17 landing site. Earth Sp. Sci. **6**, 59–95 (2019). https://doi.org/10.1029/2018EA000408

B. Hapke, *Theory of Reflectance and Emittance Spectroscopy, Topics in Remote Sensing* (Cambridge University Press, Cambridge, 1993). https://doi.org/10.1017/CBO9780511524998

B. Hapke, Bidirectional reflectance spectroscopy: 3. Correction for macroscopic roughness. Icarus **59**, 41–59 (1984)

B. Hapke, Bidirectional reflectance spectroscopy: 1. Theory. J. Geophys. Res. Solid Earth **86**, 3039–3054 (1981)

B. Hapke, An improved theoretical lunar photometric function. Astron. J. **71**, 333 (1966)

B. Hapke, B. Denevi, H. Sato, S. Braden, M. Robinson, The wavelength dependence of the lunar phase curve as seen by the Lunar Reconnaissance Orbiter wide-angle camera. J. Geophys. Res. Planets (2012). https://doi.org/10.1029/2011JE003916

B.W. Hapke, A theoretical photometric function for the lunar surface. J. Geophys. Res. **68**, 4571–4586 (1963)

P. Helfenstein, J. Veverka, Photometric properties of lunar terrains derived from Hapke's equation. Icarus **72**, 342–357 (1987)

M.D. Hicks, B.J. Buratti, J. Nettles, M. Staid, J. Sunshine, C.M. Pieters, S. Besse, J. Boardman, A photometric function for analysis of lunar images in the visual and infrared based on Moon Mineralogy Mapper observations. J. Geophys. Res. E Planets **116**, 1–10 (2011). https://doi.org/10.1029/2010JE003733

J.K. Hillier, B.J. Buratti, K. Hill, Multispectral photometry of the Moon and absolute calibration of the Clementine UV/Vis camera. Icarus **141**, 205–225 (1999). https://doi.org/10.1006/icar.1999.6184

P.J. Isaacson, C.M. Pieters, S. Besse, R.N. Clark, J.W. Head, R.L. Klima, J.F. Mustard, N.E. Petro, M.I. Staid, J.M. Sunshine, L.A. Taylor, K.G. Thaisen, S. Tompkins, Remote compositional analysis of lunar olivine-rich lithologies with Moon Mineralogy Mapper (M3) spectra. J. Geophys. Res. E Planets **116**, 1–17 (2011). https://doi.org/10.1029/2010JE003731

P. Kaur, S. Bhattacharya, P. Chauhan, A.S. Ajai Kiran Kumar, Mineralogy of Mare Serenitatis on the near side of the Moon based on Chandrayaan-1 Moon Mineralogy Mapper (M 3) observations. Icarus **222**, 137–148 (2013). https://doi.org/10.1016/j.icarus.2012.10.020

A.S. Kiran Kumar, A.R. Chowdhury, Terrain mapping camera for Chandrayaan-1. J. Earth Syst. Sci. **114**, 717–720 (2005a). https://doi.org/10.1007/BF02715955

A.S. Kiran Kumar, A.R. Chowdhury, Hyper-spectral imager in visible and near-infrared band for lunar compositional mapping. J. Earth Syst. Sci. **114**, 721–724 (2005b). https://doi.org/10.1007/BF02715956
A.S. Kiran Kumar, A.R. Chowdhury, A. Banerjee, A.B. Dave, B.N. Sharma, K.J. Shah, K.R. Murali, S.R. Joshi, S.S. Sarkar, V.D. Patel, Terrain mapping camera: a stereoscopic high-resolution instrument on Chandrayaan-1. Curr. Sci. **96**, 492–495 (2009a)
A.S. Kiran Kumar, A. Roy Chowdhury, K.R. Murali, S.S. Sarkar, S.R. Joshi, S. Mehta, A.B. Dave, K.J. Shah, A. Banerjee, K. Mathew, The hyper spectral imager instrument on Chandrayaan-1. in Lunar and Planetary Science Conference (2009b)
V. Korokhin, Y. Velikodsky, Y. Shkuratov, V. Kaydash, U. Mall, G. Videen, Using LROC WAC data for Lunar surface photoclinometry. Planet. Space Sci. **160**, 120–135 (2018). https://doi.org/10.1016/j.pss.2018.05.020
G.Y. Kramer, S. Besse, D. Dhingra, J. Nettles, R. Klima, I. Garrick-Bethell, R.N. Clark, J.P. Combe, J.W. Head, L.A. Taylor, C.M. Pieters, J. Boardman, T.B. McCord, M3 spectral analysis of lunar swirls and the link between optical maturation and surface hydroxyl formation at magnetic anomalies. J. Geophys. Res. E Planets **116**, 1–20 (2011). https://doi.org/10.1029/2010JE003729
M.A. Kreslavsky, Y.G. Shkuratov, Y.I. Velikodsky, V.G. Kaydash, D.G. Stankevich, C.M. Pieters, Photometric properties of the lunar surface derived each of which was observed. J. Geophys. Res. **105**, 20281–20296 (2000)
S. Li, P.G. Lucey, R.E. Milliken, P.O. Hayne, E. Fisher, J.-P. Williams, D.M. Hurley, R.C. Elphic, Direct evidence of surface exposed water ice in the lunar polar regions. Proc. Natl. Acad. Sci. **115**, 8907–8912 (2018). https://doi.org/10.1073/pnas.1802345115
S. Li, R.E. Milliken, Water on the surface of the Moon as seen by the Moon Mineralogy Mapper: Distribution, abundance, and origins. Sci. Adv. **3**, e1701471 (2017). https://doi.org/10.1126/sciadv.1701471
J. Longhi, D. Walker, T.L. Grove, E. Stolper, J.F. Hays, The petrology of the Apollo 17 mare basalts. in Lunar and Planetary Science Conference Proceedings. pp. 447–469 (1974)
P.G. Lucey, D.T. Blewett, B.L. Jolliff, Lunar iron and titanium abundance algorithms based on final processing of Clementine ultraviolet-visible images. J. Geophys. Res. Planets **105**, 20297–20305 (2000)
P.G. Lucey, G.J. Taylor, E. Malaret, Abundance and distribution of iron on the Moon. Science **80**(268), 1150–1153 (1995)
S. Lundeen, S.A. McLaughlin, R. Alanis, *Chandrayaan-1 Moon Mineralogy Mapper Data Product Software Interface Specifications* (Jet Propulsion Laboratory, California, 2011)
U. Mall, C. Wöhler, A. Grumpe, R. Bugiolacchi, M. Bhatt, Characterization of lunar soils through spectral features extraction in the NIR. Adv. Sp. Res. **54**, 2029–2040 (2013)
A.S. McEwen, Summary of radiometric calibration and photometric normalization steps for the Clementine UVVIS images. in Lunar and Planetary Science Conference (1998)
A.S. McEwen, A precise lunar photometric function. in Lunar and Planetary Science Conference,vol. 27, p. 841 (1996)
A.S. McEwen, Photometric functions for photoclinometry and other applications. Icarus **92**, 298–311 (1991). https://doi.org/10.1016/0019-1035(91)90053-V
R.E. Milliken, S. Li, Remote detection of widespread indigenous water in lunar pyroclastic deposits. Nat. Geosci. **10**, 561 (2017)
M.J. O'Hara, Feldspathic mare basalts at the apollo 17 landing site. Taurus-Littrow. J. Pet. **42**, 1401–1427 (2001)
M. Ohtake, T. Matsunaga, Y. Yokota, S. Yamamoto, Y. Ogawa, T. Morota, C. Honda, J. Haruyama, K. Kitazato, H. Takeda, A. Iwasaki, R. Nakamura, T. Hiroi, S. Kodama, H. Otake, Deriving the absolute reflectance of lunar surface using SELENE (Kaguya) multiband imager data. Space Sci. Rev. **154**, 57–77 (2010). https://doi.org/10.1007/s11214-010-9689-0
M. Ohtake, C.M. Pieters, P. Isaacson, S. Besse, Y. Yokota, T. Matsunaga, J. Boardman, S. Yamomoto, J. Haruyama, M. Staid, One Moon, many measurements 3: spectral reflectance. Icarus **226**, 364–374 (2013)
C.M. Pieters, Strength of mineral absorption features in the transmitted component of near-infrared reflected light: first results from RELAB. J. Geophys. Res. Solid Earth **88**, 9534–9544 (1983)
C.M. Pieters, J. Boardman, B. Buratti, A. Chatterjee, R. Clark, T. Glavich, R. Green, J. Head III., P. Isaacson, E. Malaret, T. Mccord, J. Mustard, N. Petro, C. Runyon, M. Staid, J. Sunshine, L. Taylor, S. Tompkins, P. Varanasi, M. White, The Moon mineralogy mapper (M3) on. Curr. Sci. **96**, 1–6 (2009a)
C.M. Pieters, J.W. Boardman, M. Ohtake, T. Matsunaga, J. Haruyama, R.O. Green, U. Mall, M.I. Staid, P.J. Isaacson, Y. Yokota, One Moon, many measurements 1: radiance values. Icarus **226**, 951–963 (2013)

C.M. Pieters, J.N. Goswami, R.N. Clark, M. Annadurai, J. Boardman, B. Buratti, J.-P. Combe, M.D. Dyar, R. Green, J.W. Head, Character and spatial distribution of OH/H2O on the surface of the Moon seen by M3 on Chandrayaan-1. Science **326**(80), 568–572 (2009b)
C.M. Pieters, T. Hiroi, RELAB (Reflectance Experiment Laboratory): a NASA multiuser spectroscopy facility. in Lunar and Planetary Science Conference (2004)
M.S. Robinson, B.L. Jolliff, Apollo 17 landing site: topography, photometric corrections, and heterogeneity of the surrounding highland massifs. J. Geophys. Res. **107**(E110), 5110 (2002). https://doi.org/10.1029/2001JE001614
S. Sandmeier, K.I. Itten, A physically-based model to correct atmospheric and illumination effects in optical satellite data of rugged terrain. IEEE Trans. Geosci. Remote Sens. **35**, 708–717 (1997)
H. Sato, B.W. Denevi, M.S. Robinson, B.W. Hapke, A.S. McEwen, Photometric normalization of LROC WAC global color mosaic. in EPSC-DPS Joint Meeting (2011)
H. Sato, M.S. Robinson, B. Hapke, B.W. Denevi, A.K. Boyd, Resolved Hapke parameter maps of the Moon. J. Geophys. Res. E Planets **119**, 1775–1805 (2014). https://doi.org/10.1002/2013JE004580
H.H. Schmitt, Apollo 17 report on the valley of Taurus-Littrow. Science **182**(80), 681–690 (1973)
H.H. Schmitt, N.E. Petro, R.A. Wells, M.S. Robinson, B.P. Weiss, C.M. Mercer, Revisiting the field geology of Taurus-Littrow. Icarus **298**, 2–33 (2017)
Y. Shkuratov, V. Korokhin, V. Shevchenko, O. Mikhalchenko, I. Belskaya, V. Kaydash, G. Videen, E. Zubko, Y. Velikodsky, A photometric function of planetary surfaces for gourmets. Icarus **302**, 213–236 (2018). https://doi.org/10.1016/j.icarus.2017.11.005
Y. Shkuratov, L. Starukhina, H. Hoffmann, G. Arnold, A model of spectral albedo of particulate surfaces—implications for optical properties of the. Moon **246**, 235–246 (1999a)
Y.G. Shkuratov, V.G. Kaydash, N.V. Opanasenko, Iron and titanium abundance and maturity degree distribution on the lunar nearside. Icarus **137**, 222–234 (1999b)
Yu.G. Shkuratov, M.A. Kreslavsky, A.A. Ovcharenko, D.G. Stankevich, E.S. Zubko, C. Pieters, G. Arnold, Opposition effect from Clementine data and mechanisms of backscatter. Icarus **141**, 132–155 (1999c)
G.A. Snyder, D.-C. Lee, L.A. Taylor, A.N. Halliday, E.A. Jerde, Evolution of the upper mantle of the Earth's Moon: neodymium and strontium isotopic constraints from high-Ti mare basalts. Geochim. Cosmochim. Acta **58**, 4795–4808 (1994)
R. Sridharan, S.M. Ahmed, T.P. Das, P. Sreelatha, P. Pradeepkumar, N. Naik, G. Supriya, 'Direct'evidence for water (H_2O) in the sunlit lunar ambience from CHACE on MIP of Chandrayaan I. Planet. Space Sci. **58**, 947–950 (2010)
N. Srivastava, I. Varatharajan, Geomorphology of Lowell crater region on the Moon. Icarus **266**, 44–56 (2016). https://doi.org/10.1016/j.icarus.2015.11.013
M.I. Staid, C.M. Pieters, Mineralogy of the last lunar basalts: results from Clementine. J. Geophys. Res. Planets **106**, 27887–27900 (2001)
M.I. Staid, C.M. Pieters, S. Besse, J. Boardman, D. Dhingra, R. Green, J.W. Head, P. Isaacson, R. Klima, G. Kramer, J.M. Mustard, C. Runyon, J. Sunshine, L.A. Taylor, The mineralogy of late stage lunar volcanism as observed by the Moon mineralogy mapper on Chandrayaan-1. J. Geophys. Res. E Planets **116**, 1–15 (2011). https://doi.org/10.1029/2010JE003735
I. Varatharajan, N. Srivastava, S.V.S. Murty, Mineralogy of young lunar mare basalts: assessment of temporal and spatial heterogeneity using M3 data from Chandrayaan-1. Icarus **236**, 56–71 (2014). https://doi.org/10.1016/j.icarus.2014.03.045
Y.I. Velikodsky, V.V. Korokhin, Y.G. Shkuratov, V.G. Kaydash, G. Videen, Opposition effect of the Moon from LROC WAC data. Icarus **275**, 1–15 (2016). https://doi.org/10.1016/j.icarus.2016.04.005
Y.I. Velikodsky, N.V. Opanasenko, L.A. Akimov, V.V. Korokhin, Y.G. Shkuratov, V.G. Kaydash, G. Videen, S.A. Ehgamberdiev, N.E. Berdalieva, New Earth-based absolute photometry of the Moon. Icarus **214**, 30–45 (2011). https://doi.org/10.1016/j.icarus.2011.04.021
W.L. Wang, S. Lin, CMOS sensor for RSI applications. in H. Shimoda, X. Xiong, C. Cao, X. Gu, C. Kim, A.S.K. Kumar (eds) Earth observing missions and sensors: development, implementation, and characterization II. SPIE, pp. 16–29 (2012).
S. Wentworth, G.J. Taylor, R.D. Warner, K. Keil, M.-S. Ma, R.A. Schmitt, The unique nature of Apollo 17 VLT mare basalts in Lunar and Planetary Science Conference Proceedings. pp. 207–223 (1979)
E.W. Wolfe, B.K. Lucchitta, V.S. Reed, G.E. Ulrich, A.G. Sanchez, Geology of the Taurus-Littrow valley floor. in Lunar and Planetary Science Conference Proceedings. pp. 2463–2482 (1975)
Y. Wu, S. Besse, J.-Y. Li, J.-P. Combe, Z. Wang, X. Zhou, C. Wang, Photometric correction and in-flight calibration of Chang' E-1 interference imaging spectrometer (IIM) data. Icarus **222**, 283–295 (2013). https://doi.org/10.1016/J.ICARUS.2012.11.010

Y. Wu, B. Xue, B. Zhao, P. Lucey, J. Chen, X. Xu, C. Li, Z. Ouyang, Global estimates of lunar iron and titanium contents from the Chang' E-1 IIM data. J. Geophys. Res. **117**, E02001 (2012). https://doi.org/10.1029/2011JE003879

X. Xu, J. Liu, D. Liu, B. Liu, R. Shu, Photometric correction of chang'e-1 interference imaging spectrometer's (Iim) limited observing geometries data with hapke model. Remote Sens. **12**, 1–11 (2020). https://doi.org/10.3390/rs12223676

Y. Yokota, T. Matsunaga, M. Ohtake, J. Haruyama, R. Nakamura, S. Yamamoto, Y. Ogawa, T. Morota, C. Honda, K. Saiki, K. Nagasawa, K. Kitazato, S. Sasaki, A. Iwasaki, H. Demura, N. Hirata, T. Hiroi, R. Honda, Y. Iijima, H. Mizutani, Lunar photometric properties at wavelengths 0.5–1.6 μm acquired by SELENE Spectral Profiler and their dependency on local albedo and latitudinal zones. Icarus **215**, 639–660 (2011). https://doi.org/10.1016/J.ICARUS.2011.07.028

J. Zhang, Z. Ling, W. Zhang, X. Ren, C. Li, J. Liu, Photometric modeling of the Moon using Lommel-Seeliger function and Chang'E-1 IIM data. Chin. Sci. Bull. **58**, 4588–4592 (2013)

X. Zhang, Y. Wu, Z. Ouyang, R. Bugiolacchi, Y. Chen, X. Zhang, W. Cai, A. Xu, Z. Tang, Mineralogical variation of the late stage mare basalts. J. Geophys. Res. Planets **121**, 2063–2080 (2016). https://doi.org/10.1002/2016JE005051